Japanese Journal of Applied Physics

REGULAR PAPER

Crystal structure, magnetism, and thermoelectric properties of $Nd_{1-x}Sr_xFeO_{3-\delta}$ ($0.1 \leq x \leq 0.9$)

To cite this article: Hiroshi Nakatsugawa *et al* 2023 *Jpn. J. Appl. Phys.* **62** 043001

Japanese Journal of Applied Physics **62**, 043001 (2023) **REGULAR PAPER**
https://doi.org/10.35848/1347-4065/acc9f3

Crystal structure, magnetism, and thermoelectric properties of $Nd_{1-x}Sr_xFeO_{3-\delta}$ ($0.1 \leqslant x \leqslant 0.9$)

Hiroshi Nakatsugawa[1*], Yudai Kamatani[1], Yoichi Okamoto[2], and Charles H. Hervoches[3]

[1]*Yokohama National University, Japan*
[2]*National Defense Academy, Japan*
[3]*Nuclear Physics Institute, v.v.i., ASCR Department of Neutron Physics, Czech Republic*

[*]E-mail: nakatsugawa-hiroshi-dx@ynu.ac.jp

Received January 16, 2023; revised March 25, 2023; accepted April 2, 2023; published online April 26, 2023

Polycrystalline $Nd_{1-x}Sr_xFeO_{3-\delta}$ ($0.1 \leqslant x \leqslant 0.9$) samples exhibit a single-phase perovskite-type crystal structure and G-type antiferromagnetism with small ferromagnetic order. Assuming that the Fe site is in the mixed-valence state, the spin state of Fe changes from a low-spin (LS) or intermediate spin Fe^{3+}-dominant state at $x \leqslant 0.5$ to a LS Fe^{4+} dominant state at $x \geqslant 0.6$. This strongly suggests that the charge carriers change from holes to electrons. In fact, at temperatures less than 500 K, these samples show a *p*-type Seebeck coefficient for $0.1 \leqslant x \leqslant 0.5$ and an *n*-type Seebeck coefficient for $0.6 \leqslant x \leqslant 0.9$. However, for $0.6 \leqslant x \leqslant 0.9$, Fe^{4+} is reduced to Fe^{3+} because of an oxygen deficiency in the 500–600 K temperature range. In particular, $Nd_{0.7}Sr_{0.3}FeO_{2.99(1)}$ shows the largest *p*-type $ZT = 0.025$ at 765 K, whereas compositions with high *n*-type *ZT* could not be identified. © 2023 The Japan Society of Applied Physics

1. Introduction

Bi_2Te_3,[1)] PbTe,[2)] Si–Ge alloys,[3)] skutterudites,[4,5)] and β-$FeSi_2$[6,7)] are known to be semiconductor materials with significant Seebeck coefficients, low electrical resistivity, and low thermal conductivity. However, there is a strong demand for thermoelectric materials composed of more environmentally friendly and naturally abundant elements because many contain toxic and rare metals. In recent years, various oxides have attracted attention as candidates for next-generation thermoelectric materials that are chemically stable in the air at high temperatures, environmentally friendly, and composed of abundant elements.

The thermoelectric properties of oxides have attracted attention because of the high *p*-type thermoelectric properties of Na_xCoO_2 discovered by Terasaki et al. in 1997.[8)] In addition, a series of misfit layered Co oxides[9–20)] represented by $[Ca_2CoO_3]_{0.62}CoO_2$ exhibited good p-type thermoelectric properties. Thermoelectric oxides that exhibit good *n*-type thermoelectric properties include Al-doped ZnO,[21–23)] which is a wide-bandgap degenerate semiconductor, and the strongly correlated electron system $CaMnO_3$ with partially substituted cation sites.[24–32)] No oxide with the same composition has shown *p*-type and *n*-type thermoelectric properties, as observed in the cases of Bi_2Te_3, PbTe, the Si–Ge alloy, skutterudites, and β-$FeSi_2$.[1–7)] However, some perovskite-type oxides in which transition-metal ions are in a mixed-valence state of trivalent and tetravalent ions (e.g. *n*-type perovskite type oxides such as $SrTiO_3$[33–40)] or $CaMnO_3$[24–32)] and *p*-type perovskite-type oxides such as $LaFeO_3$[41–45)] or $LaCoO_3$[46–54)]) potentially have both good *p*-type and *n*-type thermoelectric properties.

In particular, Fe^{3+} ions can exhibit a low-spin (LS) (t_{2g}^5, $g_3 = 6$), intermediate-spin (IS) ($t_{2g}^4e_g^1$, $g_3 = 24$), or a high-spin (HS) ($t_{2g}^3e_g^2$, $g_3 = 6$) configuration, and Fe^{4+} ions can have a LS (t_{2g}^4, $g_4 = 9$) or a HS ($t_{2g}^3e_g^1$, $g_4 = 10$) configuration, where g_3 and g_4 are the spin–orbital degrees of freedom for the 3*d* electrons in the trivalent and tetravalent Fe ions, respectively. In addition, using the high-temperature limit equation for the Seebeck coefficient for Fe oxides, which is an extension of the Heikes formula derived by Koshibae et al.[55)] given by

$$S_\infty \cong -\frac{k_B}{e}\ln\left(\frac{g_3}{g_4}\frac{x}{1-x}\right), \quad (1)$$

the thermoelectric characteristics tend to be *p*-type ($S_\infty > 0$ because $g_3/g_4 = 6/9 < 1$) when Fe^{3+} and Fe^{4+} are predominantly LS at $x \leqslant 0.5$, whereas they tend to be *n*-type ($S_\infty < 0$ because $g_3/g_4 = 24/9 > 1$) when Fe^{3+} and Fe^{4+} are predominantly IS and LS at $x > 0.5$, respectively. In Eq. (1), k_B is the Boltzmann constant, *e* is the elementary charge, and *x* is the concentration of tetravalent ions. Therefore, Eq. (1) suggests that perovskite-type Fe oxides with the same composition can exhibit *p*-type or *n*-type thermoelectric properties. We prepared polycrystalline $Pr_{1-x}Sr_xFeO_3$ ($0.1 \leqslant x \leqslant 0.7$) samples and confirmed that Fe^{3+} is in an LS or IS spin state and Fe^{4+} is in an LS spin state. In particular, *p*-type thermoelectric behavior with a figure of merit (*ZT*) of 0.024 ($T = 850$ K) was observed for $x = 0.1$, and *n*-type thermoelectric behavior with a $ZT = 0.002$ ($T = 850$ K) was observed for $x = 0.7$.[56)] Because the *ZT* for the *n*-type composition is lower than that for the *p*-type composition of $Pr_{1-x}Sr_xFeO_3$ ($0.1 \leqslant x \leqslant 0.7$), the development of other perovskite-type Fe oxide systems that exhibit similar *n*-type and *p*-type thermoelectric properties is desired.

The present study aims to identify perovskite-type Fe oxides whose *n*-type and *p*-type compositions exhibit similar thermoelectric properties to confirm the feasibility of fabricating *pn* devices using oxides of the same system. We prepared polycrystalline samples of $Nd_{1-x}Sr_xFeO_{3-\delta}$ ($0.1 \leqslant x \leqslant 0.9$) and characterized both their crystal and magnetic structures at 500 K, RT, and low temperature (10 K $\leqslant T \leqslant$ 15 K) using powder neutron diffraction (PND) measurements. The motivation for selecting Sr^{2+} as a substituent for Nd^{3+} is that the ionic radius is comparable to that of Nd^{3+} for Ca^{2+} and too large for Ba^{2+} compared to Nd^{3+}. Although the chemical balance of each cation (Nd^{3+}, Sr^{2+}, Fe^{3+}, and Fe^{4+}) becomes unstable when Nd^{3+} is replaced by Sr^{2+}, the electro-neutrality condition between each cation and anion (O^{2-}) is always maintained. The oxygen deficiency δ for all the samples was determined by iodometric titration. The electrical resistivity ρ, Seebeck coefficient *S*, and thermal

conductivity κ were measured under an Ar atmosphere below 800 K. However, oxygen-deficiency-induced changes in the electrical resistivity and Seebeck coefficient at temperatures above 500 K were found for the composition range $0.6 \leqslant x \leqslant 0.9$. Thus, δ for $0.6 \leqslant x \leqslant 0.9$ was determined again by iodometric titration. In addition, the magnetic susceptibility χ for each sample was measured below 700 K to confirm the spin states of Fe^{3+} and Fe^{4+} in the mixed-valence state. The ZT values derived from the thermoelectric characteristics strongly suggest that $Nd_{1-x}Sr_xFeO_{3-\delta}$ ($0.2 \leqslant x \leqslant 0.4$) might exhibit good p-type thermoelectric properties at high temperatures. However, good n-type thermoelectric properties at high temperatures are not possible.

2. Experimental

Polycrystalline $Nd_{1-x}Sr_xFeO_{3-\delta}$ ($0.1 \leqslant x \leqslant 0.9$) was synthesized using a general solid-state reaction method. The compounds were prepared from stoichiometric mixtures of Nd_2O_3 (99.9%, Fuji Film Wako Pure Chemical Industries), $SrCO_3$ (99.99%, Fuji Film Wako Pure Chemical Industries), and Fe_2O_3 (99.9%, Fuji Film Wako Pure Chemical Industries) ground in an agate mortar with ethanol (20 mL) for 1 h and then calcined at 1273 K for 24 h in air. The calcined powder samples were pressed into pellets under a uniaxial pressure of 16 MPa and sintered at 1473 K for 48 h in an O_2 atmosphere to synthesize polycrystalline samples. The oxygen deficiency δ for the $Nd_{1-x}Sr_xFeO_{3-\delta}$ ($0.1 \leqslant x \leqslant 0.9$) samples was determined from the average value obtained from three iodometric titrations. The chemical compositions of each sample were $Nd_{0.9}Sr_{0.1}FeO_{3.00(3)}$, $Nd_{0.8}Sr_{0.2}FeO_{2.996(4)}$, $Nd_{0.7}Sr_{0.3}FeO_{2.99(1)}$, $Nd_{0.6}Sr_{0.4}FeO_{2.989(8)}$, $Nd_{0.5}Sr_{0.5}FeO_{3.00(2)}$, $Nd_{0.4}Sr_{0.6}FeO_{2.99(1)}$, $Nd_{0.3}Sr_{0.7}FeO_{2.991(9)}$, $Nd_{0.2}Sr_{0.8}FeO_{2.965(5)}$, and $Nd_{0.1}Sr_{0.9}FeO_{2.952(3)}$.

PND data for the $Nd_{1-x}Sr_xFeO_{3-\delta}$ ($0.1 \leqslant x \leqslant 0.9$) samples were collected using the medium-resolution neutron powder diffractometer (MEREDIT) at the Nuclear Physics Institute, reactor LVR-15, Czech Republic. Approximately 8 g of each sample was loaded into a cylindrical vanadium sample holder with a diameter of 10 mm for data collection at 500 K, RT, and low temperature ($10\ \mathrm{K} \leqslant T \leqslant 15\ \mathrm{K}$). Monochromatic neutrons with a wavelength λ of 1.875039 Å were obtained using a Si (311) monochromator. Intensity data were collected in the range $4° \leqslant 2\theta \leqslant 143.95°$ in steps of 0.05°. All Rietveld refinements were carried out using the RIETAN-FP program[57] for crystal structures, and the GSAS-II programs[58] for magnetic structures. Both the crystal and magnetic structures were drawn using the VESTA program.[59]

The magnetic susceptibility χ was measured using an S700X-R SQUID magnetometer (Cryogenic) in the temperature range from 5 to 300 K and an MPMS SQUID magnetometer (Quantum Design) in the temperature range from 300 to 700 K; in both measurements, an external magnetic field of 1 T was applied. The DC four-terminal method measured the electrical resistivity ρ using a ResiTest8300 apparatus (TOYO) at temperatures below 395 K and using a custom-made apparatus with the sample in an Ar atmosphere in the temperature range from 400 to 800 K. The Seebeck coefficient S was measured by a steady-state method using a ResiTest8300 apparatus (TOYO) at temperatures below 395 K and using the custom-made apparatus with the sample in an Ar atmosphere in the temperature range from 400 to 800 K. The steady-state method measured the thermal conductivity κ using a power generation efficiency characteristics evaluation system (PEM-2, ADVANCE RIKO) with the sample under an Ar atmosphere in the temperature range from 300 to 540 K. The linear thermal expansion coefficients for the $x = 0.1$ and 0.8 samples were measured using a thermomechanical analyzer (TMA8310, Rigaku) with the sample under air.

The measurements of the oxygen-deficiency-induced changes in the electrical resistivity and Seebeck coefficient at temperatures above 500 K were confirmed for samples with compositions $0.6 \leqslant x \leqslant 0.9$. Thus, after the high temperature measurement, the oxygen deficiency δ for the $Nd_{1-x}Sr_xFeO_{3-\delta}$ ($0.6 \leqslant x \leqslant 0.9$) samples was again determined from the average value of three iodometric titrations. The chemical compositions of each sample were $Nd_{0.4}Sr_{0.6}FeO_{2.824(2)}$, $Nd_{0.3}Sr_{0.7}FeO_{2.769(6)}$, $Nd_{0.2}Sr_{0.8}FeO_{2.71(1)}$, and $Nd_{0.1}Sr_{0.9}FeO_{2.62(1)}$. After the high temperature measurement, the magnetic susceptibility χ for the $Nd_{1-x}Sr_xFeO_{3-\delta}$ ($0.6 \leqslant x \leqslant 0.9$) samples was also measured again using a SQUID magnetometer.

3. Results and discussion

Figure 1 shows PND patterns ($5° \leqslant 2\theta \leqslant 140°$) for $Nd_{1-x}Sr_xFeO_{3-\delta}$ ($0.1 \leqslant x \leqslant 0.9$) samples obtained at (a) 500 K, (b) RT, and (c) low temperature ($10\ \mathrm{K} \leqslant T \leqslant 15\ \mathrm{K}$). The PND patterns for all the samples indicate a single perovskite phase. The crystal and magnetic structures at both 500 K and RT were analyzed using the monoclinic $P2_1/m$ space group for $x = 0.1$ and 0.2 and the orthorhombic $Pnma$ space group for $x \geqslant 0.3$. The crystal and magnetic structures at low temperatures were analyzed using the $P2_1/m$ space group for $x = 0.1$ and 0.2, the $Pnma$ space group for $x = 0.3$ and 0.4, and the monoclinic $C2/c$ space group for $x \geqslant 0.5$. The crystal-structure parameters and magnetic moments at 500 K, RT, and low temperature were refined by Rietveld analysis using the RIETAN-FP program[57] and the GSAS-II programs[58]; the results are summarized in Tables I(a)–I(c), respectively. In the present study, the isotropic atomic displacement parameter B in the analysis was fixed at 0.5 $Å^2$ for cations and at 1.0 $Å^2$ for oxygen ions, and Tratani's split pseudo-Voigt function was used as a profile function for fitting Bragg peak shapes for the Rietveld analysis using the RIETAN-FP program.[57] The magnetic moments for Fe sites aligned in the a-, b-, and c-axis directions were assumed to be $(M_x/\mu_B, 0, 0)$, $(0, M_y/\mu_B, 0)$, and $(0, 0, M_z/\mu_B)$, respectively, where M_x, M_y, and M_z are orthogonal coordinate components of the magnetic moment and μ_B is the Bohr magneton. The magnetic structure was determined as the magnetic moment for the Fe site with the lowest reliability factor in the weighted diffraction pattern R_{wp} for the Rietveld analysis using the GSAS-II programs.[58] The BO_6 oxygen octahedron in the ABO_3 perovskite structure is a $Fe1O1_2O2_4$ type in the orthorhombic ($Pnma$) and monoclinic ($C2/c$) compounds with $x \geqslant 0.3$. A combination of $Fe1O2_2O3_2O4_2$ and $Fe2O1_2O3_2O4_2$ types in the monoclinic ($P2_1/m$) compounds with $x \leqslant 0.2$ because two kinds of Fe sites [i.e. Fe1: 2b (0.5, 0, 0) and Fe2: 2c (0, 0, 0.5)] exist in $P2_1/m$ monoclinic crystals. Two Fe sites also exist in the magnetic structures ($C2'/n'$) of monoclinic ($C2/c$) crystals. Here, O1 for the orthorhombic crystals ($Pnma$), O1 for the monoclinic crystals ($C2/c$), or O1 and O2 for monoclinic crystals ($P2_1/m$) are oxygen atoms along the central axis direction, and O2 for the

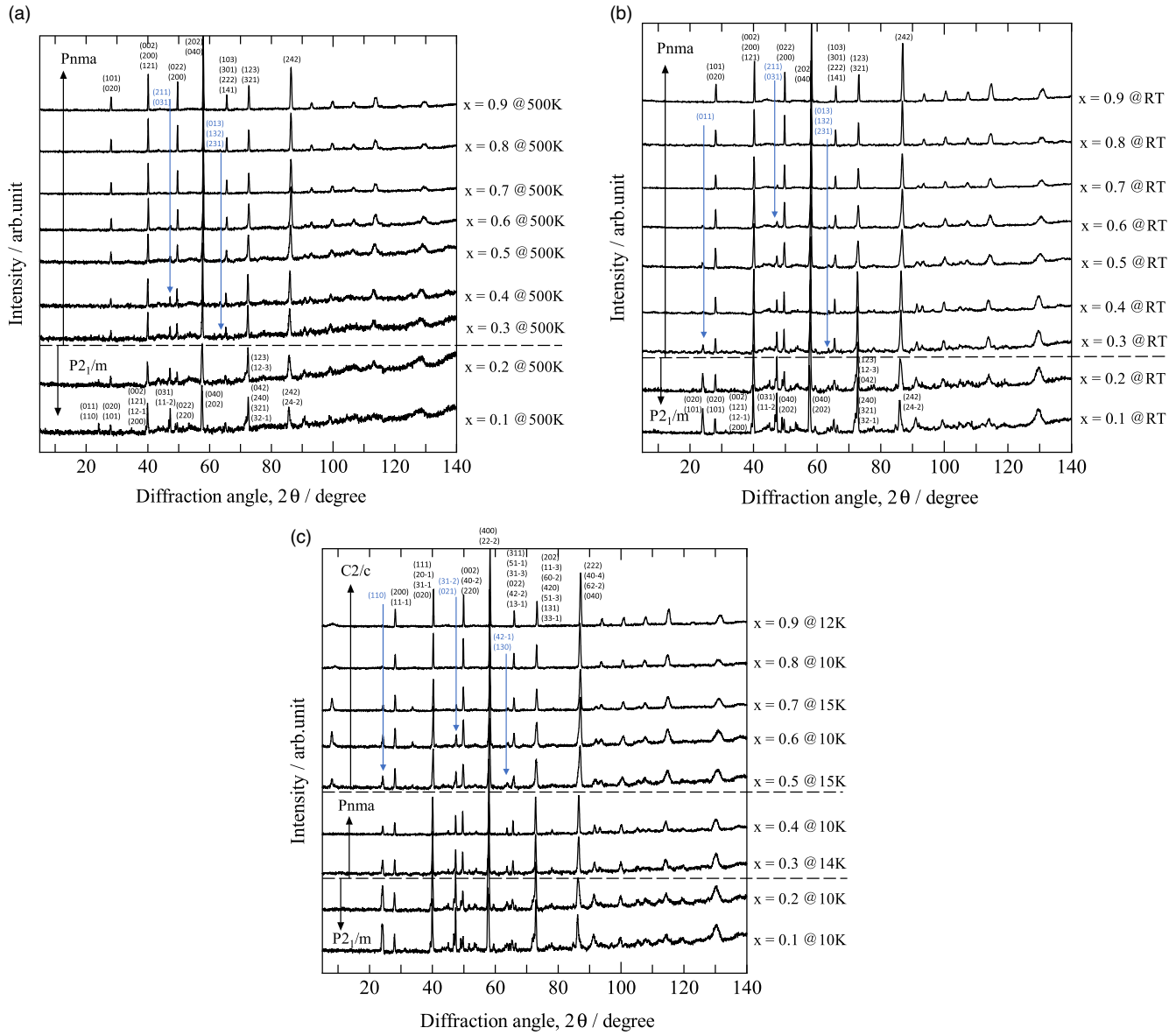

Fig. 1. (a) PND patterns for $Nd_{1-x}Sr_xFeO_{3-\delta}$ ($0.1 \leqslant x \leqslant 0.9$) at high temperature (500 K). (b) PND patterns for $Nd_{1-x}Sr_xFeO_{3-\delta}$ ($0.1 \leqslant x \leqslant 0.9$) at RT (300 K). (c) PND patterns for $Nd_{1-x}Sr_xFeO_{3-\delta}$ ($0.1 \leqslant x \leqslant 0.9$) at low temperatures (10 K $\leqslant T \leqslant$ 15 K).

orthorhombic crystals (*Pnma*), O2 for monoclinic crystals (*C*2/*c*), or O3 and O4 for monoclinic crystals ($P2_1/m$) are oxygen atoms along the direction perpendicular to the central axis.

The Fe1–O1 or Fe1–O2 distances and Fe1–O1–Fe1 or Fe1–O2–Fe1 angles indicate the degree of distortion of the orthorhombic (*Pnma*) or monoclinic (*C*2/*c*) oxygen octahedra $Fe1O1_2O2_4$. By contrast, the Fe1–O2, Fe1–O3, Fe1–O4, Fe2–O1, Fe2–O3, or Fe2–O4 distances and Fe2–O1–Fe2, Fe1–O2–Fe2, Fe2–O3–Fe1, or Fe2–O4–Fe1 angles indicate the degree of distortion of the monoclinic ($P2_1/m$) oxygen octahedra $Fe1O2_2O3_2O4_2$ and $Fe2O1_2O3_2O4_2$. The Goldschmidt tolerance factors $(r_A + r_O)/\sqrt{2}(r_B + r_O)$ and the polyhedral volume ratio V_A/V_B are summarized in Tables I(a)–I(c). Here, r_A, r_B, and r_O are the average ionic radii of the cations at the *A* and *B* sites and the radius of the oxygen ions, respectively, and V_A and V_B are the volumes of the oxygen dodecahedron AO_{12} and oxygen octahedron BO_6, respectively. The value of r_A increases, and that of r_B decreases with increasing *x*, and the Goldschmidt tolerance factor increases from 0.93 ($x = 0.1$) to 1.00 ($x = 0.9$) with increasing *x*. This tendency suggests that the strain in the FeO_6 oxygen octahedron is relaxed and that the crystal structure approaches the ideal perovskite structure. The polyhedral volume ratio V_A/V_B also increases with increasing *x*. The Howard–Stokes diagram for disordered ABO_3 perovskites[60] suggests that the crystal structure undergoes a phase transition from the monoclinic $P2_1/m$ structure to the orthorhombic *Pnma* or monoclinic *C*2/*c* structure as V_A/V_B increase.

Figure 2 shows the *x* dependence of the lattice constants for the quasi-cubic monoclinic ($P2_1/m$), orthorhombic (*Pnma*), and monoclinic (*C*2/*c*) structures at (a) 500 K, (b) RT, and (c) low temperature. A significant difference was found between $a/\sqrt{2}$ and $b/2$ in monoclinic crystals ($P2_1/m$) with $x \leqslant 0.2$; however, $a/\sqrt{2}$ and $b/2$ became almost equal in orthorhombic (*Pnma*) crystals with $x \geqslant 0.3$ at both 500 K and RT. In addition, $c/\sqrt{2}$ was the shortest in monoclinic crystals ($P2_1/m$) with $x \leqslant 0.2$ but longest in orthorhombic crystals (*Pnma*) with $0.5 \leqslant x \leqslant 0.7$ at both 500 K and RT. However, two lengths of $\sqrt{(a^2 - c^2)}/2$ and $\sqrt{(b^2 + c^2)}/2$ are observed for

Table I. (a) Crystal and magnetic structure parameters $Nd_{1-x}Sr_xFeO_{3-\delta}$ ($0.1 \leqslant x \leqslant 0.9$) at 500 K. (b) Crystal and magnetic structure parameters for (c) Crystal and magnetic structure parameters for $Nd_{1-x}Sr_xFeO_{3-\delta}$ ($0.1 \leqslant x \leqslant 0.9$) at 10–15 K.

Samples		$Nd_{1-x}Sr_xFeO_{3-\delta}$								
Composition, x		0.1@500 K	0.2@500 K	0.3@500 K	0.4@500 K	0.5@500 K	0.6@500 K	0.7@500 K	0.8@500 K	0.9@500 K
Space group		$P2_1/m$	$P2_1/m$	*Pnma*	*Pnma*	*Pnma*	*Pnma*	*Pnma*	*Pnma*	*Pnma*
average ionic radius of A site (Å)		1.29(5)	1.30(7)	1.32(8)	1.34(8)	1.36(8)	1.37(8)	1.39(8)	1.41(7)	1.42(5)
average ionic radius of B site (Å)		0.64(2)	0.63(2)	0.63(3)	0.62(3)	0.62(3)	0.61(3)	0.60(3)	0.60(2)	0.59(2)
Goldschmidt tolerance factor		0.93	0.94	0.95	0.96	0.97	0.98	0.98	0.99	1.00
polyhedral volume of A site V_A (Å^3)		50.774	50.867	50.448	50.024	49.550	49.139	49.316	49.291	48.447
polyhedral volume of B site V_B (Å^3)		10.888	10.668	10.298	10.097	9.883	9.753	9.815	9.800	9.773
polyhedral volume ratio V_A/V_B		4.663	4.768	4.899	4.954	5.014	5.039	5.025	5.029	4.957
a (Å)		5.591(2)	5.574(2)	5.522(3)	5.502(1)	5.493(1)	5.482(1)	5.4857(8)	5.4766(9)	5.484(2)
b (Å)		7.807(2)	7.790(2)	7.805(3)	7.795(2)	7.767(2)	7.753(1)	7.755(1)	7.7695(9)	7.770(1)
c (Å)		5.494(1)	5.494(1)	5.507(2)	5.506(1)	5.509(1)	5.496(1)	5.497(1)	5.4922(7)	5.483(2)
$a/\sqrt{2}$ (Å)		3.953	3.941	3.905	3.891	3.884	3.876	3.879	3.873	3.878
$b/2$ (Å)		3.904	3.895	3.903	3.898	3.884	3.877	3.878	3.885	3.885
$c/\sqrt{2}$ (Å)		3.885	3.885	3.894	3.893	3.895	3.886	3.887	3.884	3.877
V (Å^3)		239.9(1)	238.6(1)	237.3(2)	236.1(1)	235.1(1)	233.64(8)	233.91(6)	233.69(5)	233.7(1)
α (deg.)		90.0000	90.0000	90.0000	90.0000	90.0000	90.0000	90.0000	90.0000	90.0000
β (deg.)		90.08(1)	90.12(2)	90.0000	90.0000	90.0000	90.0000	90.0000	90.0000	90.0000
γ (deg.)		90.0000	90.0000	90.0000	90.0000	90.0000	90.0000	90.0000	90.0000	90.0000
Nd1/Sr1 ($P2_1/m$)	x	0.520(5)	0.511(8)	—	—	—	—	—	—	—
	y	1/4	1/4	—	—	—	—	—	—	—
	z	0.494(6)	0.50(1)	—	—	—	—	—	—	—
	B (Å^2)	0.5	0.5	—	—	—	—	—	—	—
	g	1.0	1.0	—	—	—	—	—	—	—
Nd2/Sr2 ($P2_1/m$)	x	0.050(5)	0.028(7)	0.009(7)	−0.011(3)	−0.003(4)	−0.001(3)	−0.022(1)	0.025(1)	0.005(1)
Nd1/Sr1 (*Pnma*)	y	1/4	1/4	1/4	1/4	1/4	1/4	1/4	1/4	1/4
	z	0.972(5)	0.98(1)	0.991(4)	1.010(8)	0.999(5)	0.996(4)	1.006(2)	0.991(2)	0.986(2)
	B (Å^2)	0.5	0.5	0.5	0.5	0.5	0.5	0.5	0.5	0.5
	g	1.0	1.0	1.0	1.0	1.0	1.0	1.0	1.0	1.0
Fe1 ($P2_1/m$)	x	1/2	1/2	—	—	—	—	—	—	—
	y	0	0	—	—	—	—	—	—	—
	z	0	0	—	—	—	—	—	—	—
	B (Å^2)	0.5	0.5	—	—	—	—	—	—	—
	g	1.0	1.0	—	—	—	—	—	—	—
Fe2 ($P2_1/m$)	x	0	0	0	0	0	0	0	0	0
Fe1 (*Pnma*)	y	0	0	0	0	0	0	0	0	0
	z	1/2	1/2	1/2	1/2	1/2	1/2	1/2	1/2	1/2
	B (Å^2)	0.5	0.5	0.5	0.5	0.5	0.5	0.5	0.5	0.5
	g	1.0	1.0	1.0	1.0	1.0	1.0	1.0	1.0	1.0
O1 ($P2_1/m$)	x	0.029(7)	0.03(1)	—	—	—	—	—	—	—
	y	1/4	1/4	—	—	—	—	—	—	—

Continued on next page.

Table I. Continued.

Samples		$Nd_{1-x}Sr_xFeO_{3-\delta}$								
Composition, x		0.1@500 K	0.2@500 K	0.3@500 K	0.4@500 K	0.5@500 K	0.6@500 K	0.7@500 K	0.8@500 K	0.9@500 K
Space group		$P2_1/m$	$P2_1/m$	*Pnma*	*Pnma*	*Pnma*	*Pnma*	*Pnma*	*Pnma*	*Pnma*
	z	0.438(7)	0.44(1)	—	—	—	—	—	—	—
	B (Å^2)	1.0	1.0	—	—	—	—	—	—	—
	g	1.0	1.0	—	—	—	—	—	—	—
O2 ($P2_1/m$)	x	0.432(6)	0.433(9)	0.50(1)	0.483(5)	0.471(4)	0.473(3)	0.495(2)	0.493(2)	0.527(2)
O1 (*Pnma*)	y	1/4	1/4	1/4	1/4	1/4	1/4	1/4	1/4	1/4
	z	0.084(8)	0.05(1)	0.030(3)	0.01(1)	0.080(2)	0.065(1)	0.035(1)	0.009(2)	−0.008(8)
	B (Å^2)	1.0	1.0	1.0	1.0	1.0	1.0	1.0	1.0	1.0
	g	1.0	1.0	1.0	1.0	1.0	1.0	1.0	1.0	1.0
O3 ($P2_1/m$)	x	0.282(5)	0.325(7)	0.294(5)	0.270(3)	0.263(4)	0.25(1)	0.268(2)	0.271(2)	0.26(1)
O2 (*Pnma*)	y	0.053(4)	0.021(4)	0.044(1)	0.048(1)	0.004(2)	0.002(2)	0.004(1)	0.012(1)	0.002(3)
	z	0.693(5)	0.701(6)	0.722(3)	0.713(3)	0.738(4)	0.75(1)	0.735(3)	0.737(2)	0.73(1)
	B (Å^2)	1.0	1.0	1.0	1.0	1.0	1.0	1.0	1.0	1.0
	g	1.0	1.0	1.0	1.0	1.0	1.0	1.0	1.0	1.0
O4 ($P2_1/m$)	x	0.194(5)	0.204(7)	—	—	—	—	—	—	—
	y	0.955(4)	0.950(3)	—	—	—	—	—	—	—
	z	0.220(5)	0.228(6)	—	—	—	—	—	—	—
	B (Å^2)	1.0	1.0	—	—	—	—	—	—	—
	g	1.0	1.0	—	—	—	—	—	—	—
Fe1–O2 (Å) ($P2_1/m$)		2.04(1)	2.00(1)	—	—	—	—	—	—	—
Fe1–O3 (Å) ($P2_1/m$)		2.11(3)	1.91(3)	—	—	—	—	—	—	—
Fe1–O4 (Å) ($P2_1/m$)		2.12(3)	2.10(4)	—	—	—	—	—	—	—
Fe2–O1 (Å) ($P2_1/m$)		1.988(7)	1.977(9)	—	—	—	—	—	—	—
Fe2–O3 (Å) ($P2_1/m$)		1.95(3)	2.13(4)	—	—	—	—	—	—	—
Fe2–O4 (Å) ($P2_1/m$)		1.91(2)	1.91(4)	—	—	—	—	—	—	—
Fe1–O1 (Å) (*Pnma*)		—	—	1.958(2)	1.952(2)	1.998(3)	1.976(2)	1.946(1)	1.9435(5)	1.949(1)
Fe1–O2 (Å) (*Pnma*)		—	—	2.06(3)	2.05(2)	1.95(2)	1.95(3)	1.96(2)	1.98(1)	1.94(9)
Fe1–O2 (Å) (*Pnma*)		—	—	1.93(3)	1.93(2)	1.93(2)	1.92(3)	1.92(2)	1.90(1)	1.93(9)
Fe2–O1–Fe2 (deg.) ($P2_1/m$)		158(2)	160(3)	—	—	—	—	—	—	—
Fe1–O2–Fe1 (deg.) ($P2_1/m$)		145(2)	152(2)	—	—	—	—	—	—	—
Fe2–O3–Fe1 (deg.) ($P2_1/m$)		148(1)	150(1)	—	—	—	—	—	—	—
Fe2–O4–Fe1 (deg.) ($P2_1/m$)		152(1)	153(1)	—	—	—	—	—	—	—
Fe1–O1–Fe1 (deg.) (*Pnma*)		—	—	170(1)	172(2)	152.6(7)	157.4(5)	168.5(6)	176.1(8)	170.7(9)
Fe1–O2–Fe1 (deg.) (*Pnma*)		—	—	154.3(5)	154.6(6)	173(1)	178(2)	172.1(4)	170.1(3)	172.7(5)
R_{wp} (%) for RIETAN-FP program		3.416	3.025	3.813	4.296	3.545	4.078	3.854	4.106	4.040
R_P (%) for RIETAN-FP program		2.674	2.383	3.008	3.417	2.809	3.193	2.995	3.183	3.135
R_R (%) for RIETAN-FP program		60.072	62.279	64.657	58.939	51.540	42.196	35.250	36.003	33.828
R_e (%) for RIETAN-FP program		2.134	2.045	2.480	2.232	2.301	2.495	2.468	2.461	2.470
R_B (%) for RIETAN-FP program		27.851	31.715	29.933	24.589	20.524	15.789	14.000	15.299	12.509

Continued on next page.

Table I. Continued.

Samples		$Nd_{1-x}Sr_xFeO_{3-\delta}$								
Composition, x		0.1@500 K	0.2@500 K	0.3@500 K	0.4@500 K	0.5@500 K	0.6@500 K	0.7@500 K	0.8@500 K	0.9@500 K
Space group		$P2_1/m$	$P2_1/m$	*Pnma*	*Pnma*	*Pnma*	*Pnma*	*Pnma*	*Pnma*	*Pnma*
R_F (%) for RIETAN-FP program		17.203	19.932	18.460	16.005	13.830	11.692	10.364	11.886	10.388
$S = R_{wp}/R_e$		1.601	1.479	1.538	1.925	1.541	1.634	1.562	1.668	1.636
R_{wp} (%) for GSAS-II suite programs		3.40	3.13	4.03	4.41	3.93	4.27	3.96	4.32	4.18
Fe1: [$m_x(\mu_B)$, $m_y(\mu_B)$, $m_z(\mu_B)$] ($P2_1/m$)		[0, 0, 2.1(6)]	[0, 0, 1.8(6)]	—	—	—	—	—	—	—
Fe2: [$m_x(\mu_B)$, $m_y(\mu_B)$, $m_z(\mu_B)$] ($P2_1/m$)		[0, 0, −2.6(6)]	[0, 0, −2.0(6)]	—	—	—	—	—	—	—
Fe1: [$m_x(\mu_B)$, $m_y(\mu_B)$, $m_z(\mu_B)$] (*Pnma*)		—	—	—	—	—	—	—	—	—

(b)

Samples		$Nd_{1-x}Sr_xFeO_{3-\delta}$								
Composition, x		0.1@RT	0.2@RT	0.3@RT	0.4@RT	0.5@RT	0.6@RT	0.7@RT	0.8@RT	0.9@RT
Space group		$P2_1/m$	$P2_1/m$	*Pnma*	*Pnma*	*Pnma*	*Pnma*	*Pnma*	*Pnma*	*Pnma*
Average ionic radius of A site (Å)		1.29(5)	1.30(7)	1.32(8)	1.34(8)	1.36(8)	1.37(8)	1.39(8)	1.41(7)	1.42(5)
Average ionic radius of B site (Å)		0.64(2)	0.63(2)	0.63(3)	0.62(3)	0.62(3)	0.61(3)	0.60(3)	0.60(2)	0.59(2)
Goldschmidt tolerance factor		0.93	0.94	0.95	0.96	0.97	0.98	0.98	0.99	1.00
Polyhedral volume of A site V_A (Å^3)		50.048	50.080	49.550	49.440	48.529	48.352	48.350	48.465	48.447
Polyhedral volume of B site V_B (Å^3)		10.688	10.387	10.147	10.069	9.794	9.680	9.678	9.594	9.596
Polyhedral volume ratio V_A/V_B		4.683	4.821	4.883	4.910	4.955	4.995	4.996	5.051	5.049
a (Å)		5.568(1)	5.556(2)	5.488(2)	5.478(1)	5.453(1)	5.450(1)	5.4519(9)	5.462(2)	5.4545(8)
b (Å)		7.765(2)	7.759(3)	7.755(2)	7.754(1)	7.708(2)	7.707(1)	7.713(1)	7.710(1)	7.732(1)
c (Å)		5.465(1)	5.472(2)	5.478(2)	5.480(1)	5.478(2)	5.472(1)	5.471(1)	5.457(1)	5.458(1)
$a/\sqrt{2}$ (Å)		3.937	3.929	3.881	3.874	3.856	3.854	3.855	3.862	3.857
$b/2$ (Å)		3.883	3.880	3.878	3.877	3.854	3.854	3.857	3.855	3.866
$c/\sqrt{2}$ (Å)		3.864	3.869	3.874	3.875	3.874	3.869	3.869	3.859	3.859
V (Å^3)		236.3(1)	235.9(1)	233.2(1)	232.7(1)	230.2(1)	229.8(1)	230.07(7)	229.8(1)	230.21(7)
α (deg.)		90.0000	90.0000	90.0000	90.0000	90.0000	90.0000	90.0000	90.0000	90.0000
β (deg.)		90.18(1)	90.18(1)	90.0000	90.0000	90.0000	90.0000	90.0000	90.0000	90.0000
γ (deg.)		90.0000	90.0000	90.0000	90.0000	90.0000	90.0000	90.0000	90.0000	90.0000
Nd1/Sr1 ($P2_1/m$)	x	0.511(3)	0.503(4)	—	—	—	—	—	—	—
	y	1/4	1/4	—	—	—	—	—	—	—
	z	0.501(5)	0.506(6)	—	—	—	—	—	—	—
	B (Å^2)	0.5	0.5	—	—	—	—	—	—	—
	g	1.0	1.0	—	—	—	—	—	—	—
Nd2/Sr2 ($P2_1/m$)	x	0.073(2)	0.065(3)	0.011(4)	0.013(3)	0.017(2)	−0.013(2)	−0.018(1)	−0.022(2)	0.000(1)
Nd1/Sr1 (*Pnma*)	y	1/4	1/4	1/4	1/4	1/4	1/4	1/4	1/4	1/4
	z	0.984(4)	0.980(5)	0.989(2)	0.998(4)	0.986(2)	0.996(3)	1.000(2)	1.002(6)	1.00(1)
	B (Å^2)	0.5	0.5	0.5	0.5	0.5	0.5	0.5	0.5	0.5
	g	1.0	1.0	1.0	1.0	1.0	1.0	1.0	1.0	1.0

Continued on next page.

Table I. Continued.

Samples		$Nd_{1-x}Sr_xFeO_{3-\delta}$								
Composition, x		0.1@500 K	0.2@500 K	0.3@500 K	0.4@500 K	0.5@500 K	0.6@500 K	0.7@500 K	0.8@500 K	0.9@500 K
Space group		$P2_1/m$	$P2_1/m$	*Pnma*	*Pnma*	*Pnma*	*Pnma*	*Pnma*	*Pnma*	*Pnma*
Fe1 ($P2_1/m$)	x	1/2	1/2	—	—	—	—	—	—	—
	y	0	0	—	—	—	—	—	—	—
	z	0	0	—	—	—	—	—	—	—
	B (Å^2)	0.5	0.5	—	—	—	—	—	—	—
	g	1.0	1.0	—	—	—	—	—	—	—
Fe2 ($P2_1/m$)	x	0	0	0	0	0	0	0	0	0
Fe1 (*Pnma*)	y	0	0	0	0	0	0	0	0	0
	z	1/2	1/2	1/2	1/2	1/2	1/2	1/2	1/2	1/2
	B (Å^2)	0.5	0.5	0.5	0.5	0.5	0.5	0.5	0.5	0.5
	g	1.0	1.0	1.0	1.0	1.0	1.0	1.0	1.0	1.0
O1 ($P2_1/m$)	x	0.023(5)	0.047(6)	—	—	—	—	—	—	—
	y	1/4	1/4	—	—	—	—	—	—	—
	z	0.418(6)	0.456(6)	—	—	—	—	—	—	—
	B (Å^2)	1.0	1.0	—	—	—	—	—	—	—
	g	1.0	1.0	—	—	—	—	—	—	—
O2 ($P2_1/m$)	x	0.442(4)	0.432(6)	0.495(6)	0.489(4)	0.502(5)	0.499(5)	0.505(3)	0.497(3)	0.524(1)
O1 (*Pnma*)	y	1/4	1/4	1/4	1/4	1/4	1/4	1/4	1/4	1/4
	z	0.081(6)	0.067(6)	0.031(2)	0.031(3)	0.080(2)	0.065(1)	0.045(1)	−0.021(4)	0.00(1)
	B (Å^2)	1.0	1.0	1.0	1.0	1.0	1.0	1.0	1.0	1.0
	g	1.0	1.0	1.0	1.0	1.0	1.0	1.0	1.0	1.0
O3 ($P2_1/m$)	x	0.292(3)	0.299(5)	0.293(3)	0.297(2)	0.265(3)	0.265(3)	0.267(2)	0.274(2)	0.250(4)
O2 (*Pnma*)	y	0.061(2)	0.047(2)	0.046(1)	0.042(1)	0.011(1)	0.006(1)	0.009(1)	0.002(6)	0.006(2)
	z	0.699(4)	0.701(4)	0.720(2)	0.728(2)	0.725(2)	0.735(3)	0.739(3)	0.743(4)	0.729(1)
	B (Å^2)	1.0	1.0	1.0	1.0	1.0	1.0	1.0	1.0	1.0
	g	1.0	1.0	1.0	1.0	1.0	1.0	1.0	1.0	1.0
O4 ($P2_1/m$)	x	0.211(3)	0.219(5)	—	—	—	—	—	—	—
	y	0.963(2)	0.963(2)	—	—	—	—	—	—	—
	z	0.214(4)	0.219(4)	—	—	—	—	—	—	—
	B (Å^2)	1.0	1.0	—	—	—	—	—	—	—
	g	1.0	1.0	—	—	—	—	—	—	—
Fe1–O2 (Å) ($P2_1/m$)		2.017(9)	2.010(8)	—	—	—	—	—	—	—
Fe1–O3 (Å) ($P2_1/m$)		2.06(2)	2.00(3)	—	—	—	—	—	—	—
Fe1–O4 (Å) ($P2_1/m$)		2.00(2)	1.98(3)	—	—	—	—	—	—	—
Fe2–O1 (Å) ($P2_1/m$)		1.996(8)	1.971(6)	—	—	—	—	—	—	—
Fe2–O3 (Å) ($P2_1/m$)		2.01(2)	2.02(3)	—	—	—	—	—	—	—
Fe2–O4 (Å) ($P2_1/m$)		1.98(2)	1.98(2)	—	—	—	—	—	—	—
Fe1–O1 (Å) (*Pnma*)		—	—	1.946(1)	1.946(1)	1.977(2)	1.960(1)	1.944(1)	1.931(1)	1.937(1)

Continued on next page.

Table I. Continued.

Samples	$Nd_{1-x}Sr_xFeO_{3-\delta}$								
Composition, x	0.1@500 K	0.2@500 K	0.3@500 K	0.4@500 K	0.5@500 K	0.6@500 K	0.7@500 K	0.8@500 K	0.9@500 K
Space group	$P2_1/m$	$P2_1/m$	*Pnma*	*Pnma*	*Pnma*	*Pnma*	*Pnma*	*Pnma*	*Pnma*
Fe1–O2 (Å) (*Pnma*)	—	—	2.04(2)	2.07(1)	1.97(2)	1.93(2)	1.96(1)	2.00(2)	2.00(1)
Fe1–O2 (Å) (*Pnma*)	—	—	1.93(2)	1.88(1)	1.90(2)	1.93(2)	1.90(2)	1.86(2)	1.85(1)
Fe2–O1–Fe2 (deg.) ($P2_1/m$)	152(1)	159(1)	—	—	—	—	—	—	—
Fe1–O2–Fe1 (deg.) ($P2_1/m$)	148(1)	149(1)	—	—	—	—	—	—	—
Fe2–O3–Fe1 (deg.) ($P2_1/m$)	145.6(9)	149(1)	—	—	—	—	—	—	—
Fe2–O4–Fe1 (deg.) ($P2_1/m$)	156(1)	158(1)	—	—	—	—	—	—	—
Fe1–O1–Fe1 (deg.) (*Pnma*)	—	—	169.8(8)	169(1)	154.1(6)	158.8(5)	165.2(6)	173(1)	171.8(8)
Fe1–O2–Fe1 (deg.) (*Pnma*)	—	—	153.2(4)	155.3(4)	169.4(6)	172.5(6)	172.4(5)	172.7(9)	174(1)
R_{wp} (%) for RIETAN-FP program	5.898	5.940	5.682	5.390	4.670	4.592	4.518	6.220	5.653
R_P (%) for RIETAN-FP program	4.078	4.295	4.298	4.018	3.431	3.436	3.440	5.031	4.234
R_R (%) for RIETAN-FP program	36.678	37.662	39.963	35.671	28.917	27.467	26.210	34.160	30.397
R_e (%) for RIETAN-FP program	2.419	2.304	2.327	2.339	2.303	2.303	2.308	2.323	2.317
R_B (%) for RIETAN-FP program	16.743	15.638	17.436	16.688	11.629	12.174	12.006	11.252	16.320
R_F (%) for RIETAN-FP program	8.406	7.853	9.287	10.412	6.596	7.914	9.174	8.555	11.825
$S = R_{wp}/R_e$	2.438	2.578	2.442	2.304	2.028	1.994	1.958	2.678	2.440
R_{wp} (%) for GSAS-II suite programs	5.03	6.46	6.15	5.48	6.51	5.96	4.83	6.64	5.60
Fe1: [$m_x(\mu_B)$, $m_y(\mu_B)$, $m_z(\mu_B)$] ($P2_1/m$)	[0, 0, 2.9(3)]	[0, 0, 2.5(4)]	—	—	—	—	—	—	—
Fe2: [$m_x(\mu_B)$, $m_y(\mu_B)$, $m_z(\mu_B)$] ($P2_1/m$)	[0, 0, −3.5(3)]	[0, 0, −2.9(4)]	—	—	—	—	—	—	—
Fe1: [$m_x(\mu_B)$, $m_y(\mu_B)$, $m_z(\mu_B)$] (*Pnma*)	—	—	[0, 0, 1.97(9)]	[0.8(1), 0, 0]	[1.3(1), 0, 0]	[0.9(1), 0, 0]	[0.2(2), 0, 0]	[0.5(1), 0, 0]	[0, 0, 0.2(2)]

(c)

Samples	$Nd_{1-x}Sr_xFeO_{3-\delta}$								
Composition, x	0.1@10 K	0.2@10 K	0.3@14 K	0.4@10 K	0.5@15 K	0.6@10 K	0.7@15 K	0.8@10 K	0.9@12 K
Space group	$P2_1/m$	$P2_1/m$	*Pnma*	*Pnma*	*C2/c*	*C2/c*	*C2/c*	*C2/c*	*C2/c*
Average ionic radius of A site (Å)	1.29(5)	1.30(7)	1.32(8)	1.34(8)	1.36(8)	1.37(8)	1.39(8)	1.41(7)	1.42(5)
Average ionic radius of B site (Å)	0.64(2)	0.63(2)	0.63(3)	0.62(3)	0.62(3)	0.61(3)	0.60(3)	0.60(2)	0.59(2)
Goldschmidt tolerance factor	0.93	0.94	0.95	0.96	0.97	0.98	0.98	0.99	1.00
polyhedral volume of A site V_A (Å^3)	49.688	49.661	48.844	48.898	47.591	47.503	47.486	47.760	47.451
Polyhedral volume of B site V_B (Å^3)	10.546	10.295	9.957	9.994	9.704	9.646	9.604	9.563	9.494
Polyhedral volume ratio V_A/V_B	4.711	4.824	4.905	4.893	4.904	4.924	4.944	4.994	4.998
a (Å)	5.560(1)	5.549(1)	5.483(2)	5.474(1)	9.435(8)	9.411(6)	9.405(4)	9.450(4)	9.433(3)
b (Å)	7.745(1)	7.741(1)	7.737(1)	7.735(1)	5.470(2)	5.467(1)	5.461(1)	5.451(2)	5.439(1)
c (Å)	5.451(1)	5.458(1)	5.467(1)	5.4690(6)	5.447(5)	5.438(3)	5.437(2)	5.448(2)	5.435(1)
$a/2^{0.5}$ (Å) (*Pnma*, $P2_1/m$), $(a^2–c^2)^{0.5}/2$ (*C2/c*)	3.932	3.924	3.877	3.871	3.852	3.840	3.837	3.861	3.855
$b/2$ (Å) (*Pnma*, $P2_1/m$), $(b^2 + c^2)^{0.5}/2$ (*C2/c*)	3.873	3.871	3.869	3.868	3.860	3.856	3.853	3.853	3.845
$c/2^{0.5}$(Å) (*Pnma*, $P2_1/m$), $(b^2 + c^2)^{0.5}/2$ (*C2/c*)	3.854	3.859	3.866	3.867	3.860	3.856	3.853	3.853	3.845
V (Å^3)	234.77(8)	234.5(1)	231.9(1)	231.58(6)	229(9)	228(5)	228(3)	229(5)	227(2)
α (deg.)	90.0000	90.0000	90.0000	90.0000	90.0000	90.0000	90.0000	90.0000	90.0000

Continued on next page.

Table I. Continued.

Samples		$Nd_{1-x}Sr_xFeO_{3-\delta}$								
Composition, x		0.1@500 K	0.2@500 K	0.3@500 K	0.4@500 K	0.5@500 K	0.6@500 K	0.7@500 K	0.8@500 K	0.9@500 K
Space group		$P2_1/m$	$P2_1/m$	*Pnma*	*Pnma*	*Pnma*	*Pnma*	*Pnma*	*Pnma*	*Pnma*
β (deg.)		90.180(7)	90.15(1)	90.0000	90.0000	125.40(6)	125.23(3)	125.16(2)	125.23(3)	125.23(1)
γ (deg.)		90.0000	90.0000	90.0000	90.0000	90.0000	90.0000	90.0000	90.0000	90.0000
Nd1/Sr1 ($P2_1/m$)	x	0.508(2)	0.501(3)	—	—	—	—	—	—	—
	y	1/4	1/4	—	—	—	—	—	—	—
	z	0.514(3)	0.510(3)	—	—	—	—	—	—	—
	B (Å^2)	0.5	0.5	—	—	—	—	—	—	—
	g	1.0	1.0	—	—	—	—	—	—	—
Nd2/Sr2 ($P2_1/m$)	x	0.076(2)	0.073(2)	0.023(3)	0.021(2)	0	0	0	0	0
Nd1/Sr1 (*Pnma, C2/c*)	y	1/4	1/4	1/4	1/4	0.257(2)	0.258(2)	0.257(2)	0.245(5)	0.24(3)
	z	0.976(3)	0.971(3)	0.980(1)	0.982(1)	1/4	1/4	1/4	1/4	1/4
	B (Å^2)	0.5	0.5	0.5	0.5	0.5	0.5	0.5	0.5	0.5
	g	1.0	1.0	1.0	1.0	1.0	1.0	1.0	1.0	1.0
Fe1 ($P2_1/m$)	x	1/2	1/2	—	—	—	—	—	—	—
	y	0	0	—	—	—	—	—	—	—
	z	0	0	—	—	—	—	—	—	—
	B (Å^2)	0.5	0.5	—	—	—	—	—	—	—
	g	1.0	1.0	—	—	—	—	—	—	—
Fe2 ($P2_1/m$)	x	0	0	0	0	1/4	1/4	1/4	1/4	1/4
Fe1 (*Pnma, C2/c*)	y	0	0	0	0	1/4	1/4	1/4	1/4	1/4
	z	1/2	1/2	1/2	1/2	0	0	0	0	0
	B (Å^2)	0.5	0.5	0.5	0.5	0.5	0.5	0.5	0.5	0.5
	g	1.0	1.0	1.0	1.0	1.0	1.0	1.0	1.0	1.0
O1 ($P2_1/m$)	x	0.031(3)	0.039(4)	—	—	—	—	—	—	—
	y	1/4	1/4	—	—	—	—	—	—	—
	z	0.416(4)	0.450(4)	—	—	—	—	—	—	—
	B (Å^2)	1.0	1.0	—	—	—	—	—	—	—
	g	1.0	1.0	—	—	—	—	—	—	—
O2 ($P2_1/m$)	x	0.434(3)	0.416(4)	0.503(4)	0.494(4)	0	0	0	0	0
O1 (*Pnma. C2/c*)	y	1/4	1/4	1/4	1/4	0.672(2)	0.682(2)	0.695(1)	0.75(1)	0.75(3)
	z	0.061(4)	0.050(4)	0.032(1)	0.034(1)	1/4	1/4	1/4	1/4	1/4
	B (Å^2)	1.0	1.0	1.0	1.0	1.0	1.0	1.0	1.0	1.0
	g	1.0	1.0	1.0	1.0	1.0	1.0	1.0	1.0	1.0
O3 ($P2_1/m$)	x	0.292(2)	0.307(3)	0.258(4)	0.273(3)	0.244(2)	0.243(1)	0.241(1)	0.240(4)	0.243(3)
O2 (*Pnma, C2/c*)	y	0.063(1)	0.058(1)	0.0496(7)	0.0444(6)	0.028(2)	0.017(2)	0.007(4)	0.01(1)	0.00(2)
	z	0.708(3)	0.721(3)	0.716(1)	0.720(1)	0.264(5)	0.262(4)	0.253(4)	0.25(1)	0.25(1)
	B (Å^2)	1.0	1.0	1.0	1.0	1.0	1.0	1.0	1.0	1.0
	g	1.0	1.0	1.0	1.0	1.0	1.0	1.0	1.0	1.0

Continued on next page.

Table I. Continued.

Samples		$Nd_{1-x}Sr_xFeO_{3-\delta}$								
Composition, x		0.1@500 K	0.2@500 K	0.3@500 K	0.4@500 K	0.5@500 K	0.6@500 K	0.7@500 K	0.8@500 K	0.9@500 K
Space group		$P2_1/m$	$P2_1/m$	*Pnma*	*Pnma*	*Pnma*	*Pnma*	*Pnma*	*Pnma*	*Pnma*
O4 ($P2_1/m$)	x	0.216(3)	0.235(3)	—	—	—	—	—	—	—
	y	0.958(1)	0.960(1)	—	—	—	—	—	—	—
	z	0.214(3)	0.212(3)	—	—	—	—	—	—	—
	B (Å^2)	1.0	1.0	—	—	—	—	—	—	—
	g	1.0	1.0	—	—	—	—	—	—	—
Fe1–O2 (Å) ($P2_1/m$)		1.998(5)	2.009(5)	—	—	—	—	—	—	—
Fe1–O3 (Å) ($P2_1/m$)		2.02(1)	1.90(1)	—	—	—	—	—	—	—
Fe1–O4 (Å) ($P2_1/m$)		1.99(2)	1.90(1)	—	—	—	—	—	—	—
Fe2–O1 (Å) ($P2_1/m$)		1.997(6)	1.967(4)	—	—	—	—	—	—	—
Fe2–O3 (Å) ($P2_1/m$)		2.03(1)	2.13(1)	—	—	—	—	—	—	—
Fe2–O4 (Å) ($P2_1/m$)		1.99(2)	2.06(1)	—	—	—	—	—	—	—
Fe1–O1 (Å) (*Pnma*, *C2/c*)		—	—	1.9427(9)	1.9431(8)	1.969(3)	1.957(2)	1.945(1)	1.930(1)	1.926(3)
Fe1–O2 (Å) (*Pnma*, *C2/c*)		—	—	2.07(1)	1.99(1)	1.97(2)	1.93(2)	1.94(2)	1.9(1)	1.9(1)
Fe1–O2 (Å) (*Pnma*, *C2/c*)		—	—	1.88(2)	1.95(1)	1.90(2)	1.92(2)	1.91(2)	1.9(1)	1.9(1)
Fe2–O1–Fe2 (deg.) ($P2_1/m$)		151(1)	159(1)	—	—	—	—	—	—	—
Fe1–O2–Fe1 (deg.) ($P2_1/m$)		151(1)	148(1)	—	—	—	—	—	—	—
Fe2–O3–Fe1 (deg.) ($P2_1/m$)		146.2(7)	147.4(7)	—	—	—	—	—	—	—
Fe2–O4–Fe1 (deg.) ($P2_1/m$)		155.6(8)	158.5(8)	—	—	—	—	—	—	—
Fe1–O1–Fe1 (deg.) (*Pnma*, *C2/c*)		—	—	169.3(5)	168.7(4)	154.9(6)	158.2(6)	162.2(6)	177(3)	178(12)
Fe1–O2–Fe1 (deg.) (*Pnma*, *C2/c*)		—	—	155.6(4)	156.6(3)	168.7(5)	171.0(5)	173.8(7)	173.3(6)	175(2)
R_{wp} (%) for RIETAN-FP program		5.808	5.453	5.721	4.194	5.503	6.271	6.758	4.736	4.837
R_P (%) for RIETAN-FP program		3.797	3.738	4.206	3.166	4.014	4.100	4.063	3.629	3.751
R_R (%) for RIETAN-FP program		37.779	35.937	40.600	32.776	36.659	34.982	31.083	31.504	29.274
R_e (%) for RIETAN-FP program		2.932	2.946	2.887	2.856	2.860	2.869	2.890	2.903	2.841
R_B (%) for RIETAN-FP program		14.162	12.485	10.968	10.745	9.437	10.872	7.985	7.449	7.720
R_F (%) for RIETAN-FP program		5.958	5.599	5.256	5.886	4.203	5.169	4.791	5.364	6.251
$S = R_{wp}/R_e$		1.981	1.851	1.982	1.468	1.924	2.186	2.338	1.631	1.703
R_{wp} (%) for GSAS-II suite programs		4.51	5.54	5.63	3.84	5.80	5.34	4.53	4.84	5.21
Fe1, Fe1_2: [$m_x(\mu_B)$, $m_y(\mu_B)$, $m_z(\mu_B)$] ($P2_1/m$, $C2'/n'$)		[0, 0, 4.0(1)]	[0, 0, 3.0(4)]	—	—	[0, 3.29(6), 0]	[0, 3.54(5), 0]	[0, 2.89(5), 0]	[0, 0.9(1), 0]	—
Fe2, Fe1_3: [$m_x(\mu_B)$, $m_y(\mu_B)$, $m_z(\mu_B)$] ($P2_1/m$, $C2'/n'$)		[0, 0, −3.2(1)]	[0, 0, −3.3(4)]	—	—	[0, −0.01(9), 0]	[0, −0.96(7), 0]	[0, −1.87(6), 0)]	[0, −0.2(1), 0]	—
Fe1: [$m_x(\mu_B)$, $m_y(\mu_B)$, $m_z(\mu_B)$](*Pnma*)		—	—	[0, 0, 2.96(5)]	[2.37(3), 0, 0]	—	—	—	—	—

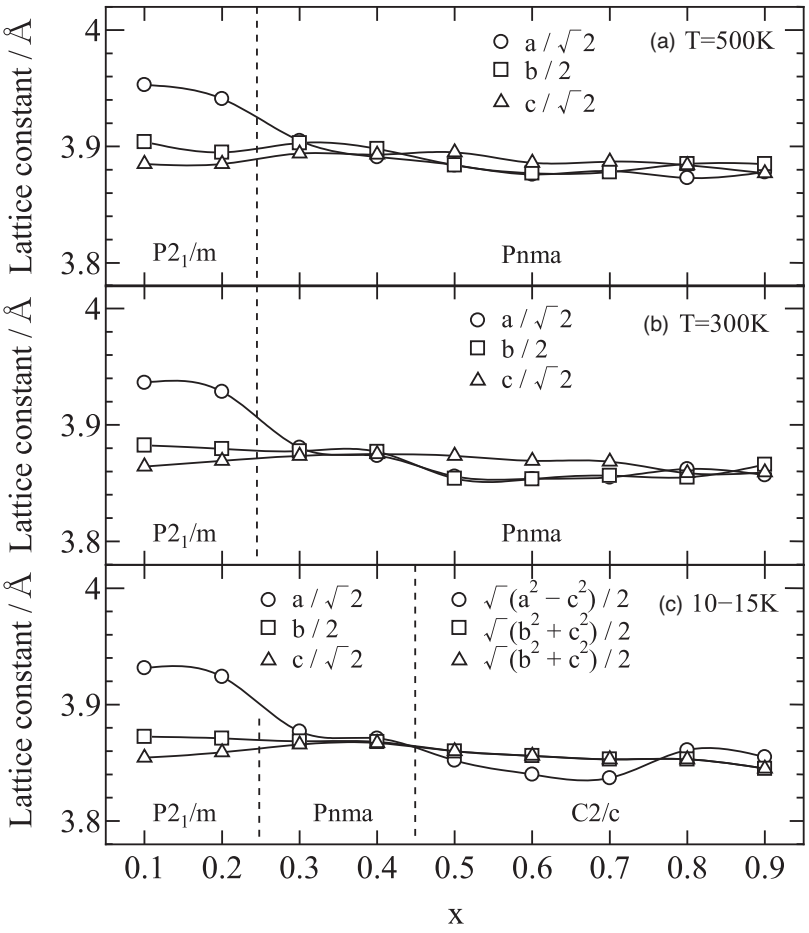

Fig. 2. Lattice constants for pseudo-cubic $Nd_{1-x}Sr_xFeO_{3-\delta}$ ($0.1 \leqslant x \leqslant 0.9$) at (a) 500 K, (b) 300 K, and (c) 10 K $\leqslant T \leqslant$ 15 K.

monoclinic crystals (*C*2/*c*) with $x \geqslant 0.5$, where the latter is larger than the former in crystals with $0.5 \leqslant x \leqslant 0.7$ at low temperatures. The reversal of this lattice constant's magnitude affects the magnetic moment's alignment direction in each sample. The magnetic structure shows G-type antiferromagnetism with small ferromagnetic order[61–63] in the *c*-axis direction for $x \leqslant 0.3$ and the *a*- or *b*-axis directions at RT or low temperature for $0.4 \leqslant x \leqslant 0.8$. However, as shown in Tables I(a)–I(c), the Fe–O–Fe angle at 500 K, RT, and low temperature tends to increase with increasing *x*. At $x \geqslant 0.8$, both the Fe1–O1–Fe1 and Fe1–O2–Fe1 angles reach 170°–180°, which suggests that the strain in the FeO_6 oxygen octahedron tends to be relaxed with increasing *x*. As shown in Table I(c), the unit cell volume at low increases from 228(3) Å^3 for $x = 0.7$ to 229(5) Å^3 for $x = 0.8$ because the lattice constant *a* increases from 9.405(4) Å for $x = 0.7$ to 9.450(4) Å for $x = 0.8$. However, the increase in unit cell volume is within the standard deviation.

Figure 3 shows the *x* dependence of the absolute value of the magnetic moment $|M|$ for the Fe site at (a) 500 K, (b) RT, and (c) low temperature, plotted as a solid line. The *x* dependence of the effective magnetic moment μ_{eff} at the Fe site, estimated from the Curie constant obtained from the temperature dependence of the reciprocal magnetic susceptibility $(\chi—\chi_0)^{-1}$ in the paramagnetic region, is shown by a broken line. Because the magnetic moments at the Fe1 site and the Fe2 site differ for the monoclinic crystals ($P2_1/m$) at 500 K, RT, and low temperature, the $|M|$ value for the Fe1 site is plotted as solid circles, and that for the Fe2 site is plotted as open circles. In the orthorhombic crystal (*Pnma*) at 500 K, $|M|$ is not plotted because we could not observe sufficient magnetic peaks to analyze the magnetic structure. For orthorhombic crystals (*Pnma*) at room and low temperatures, the value of $|M|$ for the Fe1 site is plotted as solid squares. Because the magnetic moments at the Fe1_2 site and the Fe1_3 site also differ for the monoclinic crystals (*C*2/*c*) at low temperature, the value of $|M|$ for the Fe1_2 site is plotted as solid squares, and that of $|M|$ for the Fe1_3 site is plotted as solid triangles. The μ_{eff} per Fe site estimated from the measurement of χ is plotted as open squares for all *x*. As *x* increases, $|M|$ tends to decrease; however, the μ_{eff} remains almost constant at ~2.8 μ_B. At low temperatures, a good match is observed between $|M|$ and μ_{eff} at $x \leqslant 0.7$; however, at 500 K and RT, a significant discrepancy is observed between $|M|$ and μ_{eff}, especially at RT for the samples with $x \geqslant 0.3$. This suggests that the vector sum of the magnetic moments, which should be reflected in the antiferromagnetism with small ferromagnetic order[61–63] at low temperatures, is offset by thermal scattering in the paramagnetic region at temperatures above RT.

As shown in Fig. 4(a), the crystal-structure analysis of the PND pattern for $Nd_{0.9}Sr_{0.1}FeO_{3.00(3)}$ at 10 K using the RIETAN-FP program,[57] which was performed before magnetic-structure analysis using the GSAS-II programs,[58] indicates a monoclinic ($P2_1/m$) perovskite-type single phase. As shown in Table I(c), the reliability factor R_{wp} is 5.808% for the crystal-structure analysis and 4.51% for the magnetic-structure analysis; thus, R_{wp} was improved by the Rietveld

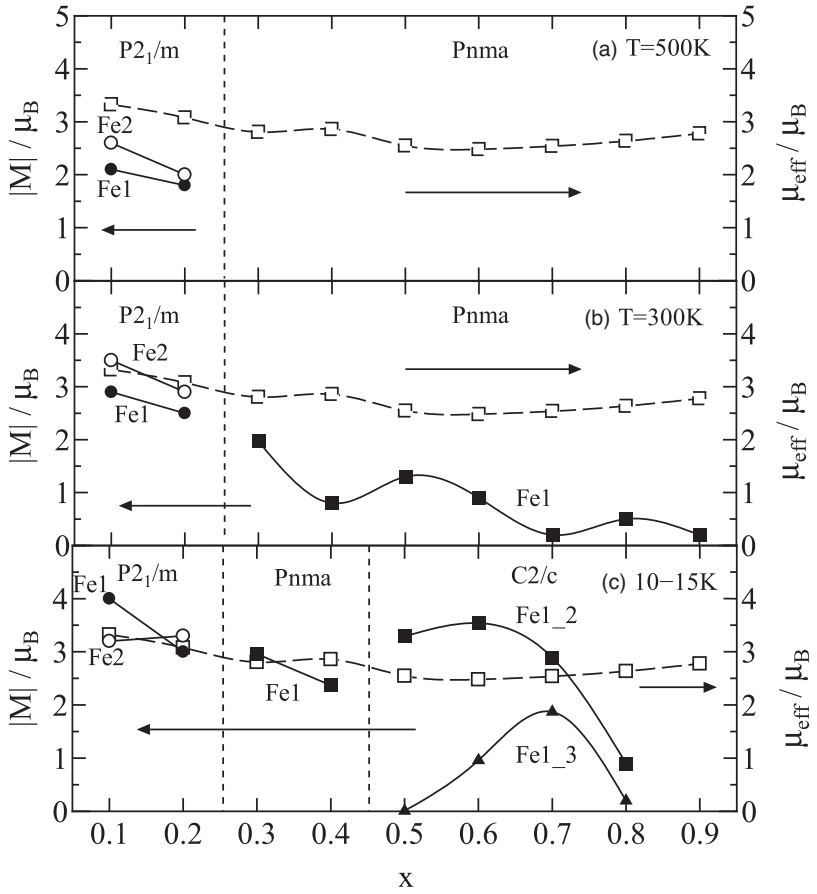

Fig. 3. Magnetic moments obtained from PND measurements at (a) 500 K, (b) 300 K, and (c) 10 K $\leqslant T \leqslant$ 15 K, and the effective magnetic moments obtained from Eq. (2) for $Nd_{1-x}Sr_xFeO_{3-\delta}$ ($0.1 \leqslant x \leqslant 0.9$).

analysis of the magnetic structure. The crystal-structure analysis in Fig. 4(a) is insufficient to fit the diffraction patterns; however, the magnetic-structure analysis in Fig. 4(b) shows the fitting results for all the diffraction patterns. The magnetic moments are aligned in G-type antiferromagnetic order in the *c*-axis direction, where $|M|$ for the Fe1 site is 4.0(1) μ_B and $|M|$ for the Fe2 site is 3.2(1) μ_B.

As shown in Fig. 5(a), the crystal-structure analysis based on the PND pattern for $Nd_{0.5}Sr_{0.5}FeO_{3.00(2)}$ at 15 K, as performed using the RIETAN-FP program,[57] which was carried out before the magnetic-structure analysis using the GSAS-II suite programs,[58] shows that it is a single-phase monoclinic (*C*2/*c*) perovskite. As shown in Table I(c), the reliability factor R_{wp} is 5.503% in the crystal-structure analysis and 5.80% in the magnetic-structure analysis; thus, the reliability factors are similar. The crystal-structure analysis in Fig. 5(a) is insufficient to fit the diffraction patterns; however, the magnetic-structure analysis in Fig. 5(b) shows the fitting results for all the diffraction patterns. The space group of the magnetic structure is $C2'/n'$, and the magnetic moment is mainly aligned in the *b*-axis direction of the Fe1_2 site, where $|M|$ for the Fe1_2 site is 3.29(6) μ_B and $|M|$ for the Fe1_3 site. is 0.01(9) μ_B.

Figures 6(a) and 6(b) show the temperature dependence of (a) the magnetic susceptibility $\chi - \chi_0$ in both warm-up and cool-down processes and (b) the inverse of the magnetic susceptibility $(\chi - \chi_0)^{-1}$ in the warm-up process for $Nd_{1-x}Sr_xFeO_{3-\delta}$ ($0.1 \leqslant x \leqslant 0.9$) samples measured in the temperature range from 5 to 700 K under a magnetic field of 1 T, where the contribution of temperature-independent magnetic susceptibility χ_0 is estimated by extrapolation in the high-temperature limit from the relationship between χ and T^{-1}. Figure 6(c) shows the temperature dependence of the magnetic susceptibility $\chi - \chi_0$ in both warm-up and cool-down processes and the inverse of the magnetic susceptibility $(\chi - \chi_0)^{-1}$ in the warm-up process for $Nd_{1-x}Sr_xFeO_{3-\delta}$ ($0.6 \leqslant x \leqslant 0.9$) samples after high-temperature measurement measured in the temperature range from 5 to 700 K under a magnetic field of 1 T. As shown in Fig. 6(a), the magnetic susceptibility anomalies around 200 K for $x = 0.6$ and $x = 0.7$ are considered to be the boundary between G-type antiferromagnetism with small ferromagnetic order on the low temperature side and paramagnetism on the high temperature side, i.e. the antiferromagnetic transition. Therefore, the inverse of the magnetic susceptibility around 200 K for $x = 0.6$ and $x = 0.7$ shows a maximum of around 150 K, as shown in Fig. 6(b). Since we have measured the magnetic susceptibility above 300 K in both warm-up and cool-down processes, the temperature dependence of the magnetic susceptibility in both warm-up and cool-down processes is shown in Figs. 6(a) and 6(c). We observed no significant change in the temperature dependence of the magnetic susceptibility above 300 K in both warm-up and cool-down processes. As is clear from the iodine titration results, samples with $x > 0.6$ show a progressive oxygen deficiency at 550–600 K after the high temperature measurement. In other words, due to oxygen deficiency, LS Fe^{4+} is

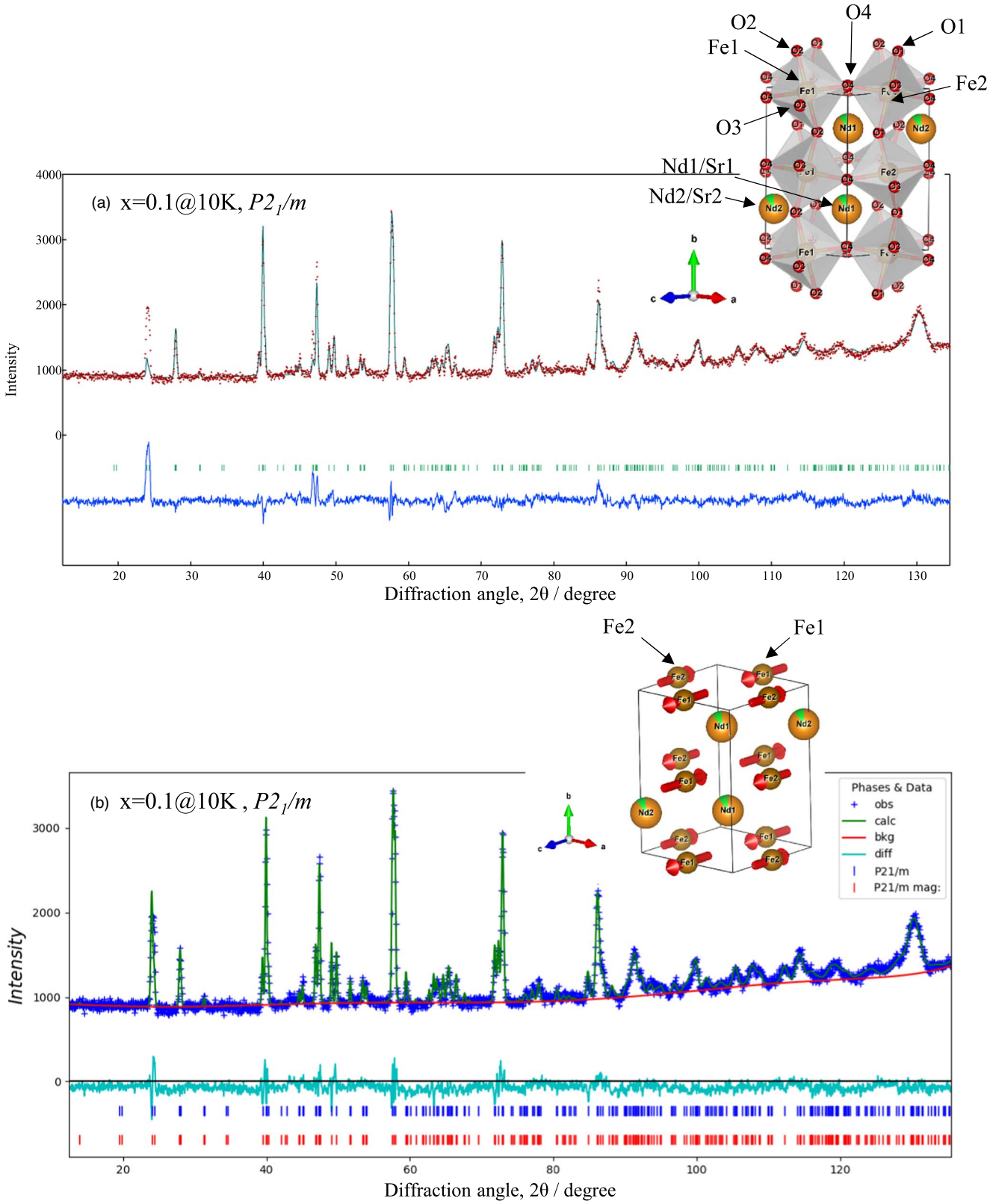

Fig. 4. (a) PND pattern and crystal structure, and (b) PND pattern and magnetic structure for $Nd_{0.9}Sr_{0.1}FeO_{3.00(3)}$ at 10 K.

reduced to IS Fe^{3+} or LS Fe^{3+} in samples for $x > 0.6$, and the conduction carrier changes from electron to hole, increasing resistivity. It strongly suggests that the effective magnetic moment μ_{eff} formed by the mixed valence states of the Fe sites (i.e. LS Fe^{4+}, IS Fe^{3+}, and LS Fe^{3+}) remains constant even with progressive oxygen deficiency in samples for $x > 0.6$.

As shown in Fig. 6(a), in all the samples, a decreasing tendency of $\chi - \chi_0$ is shown with increasing temperature, and the magnetic phase transition from low temperature G-type antiferromagnetism to high-temperature paramagnetism is confirmed. The tangents to each plot in Fig. 6(b) represent the high-temperature paramagnetic region for each sample. In general, the temperature dependence of paramagnetic

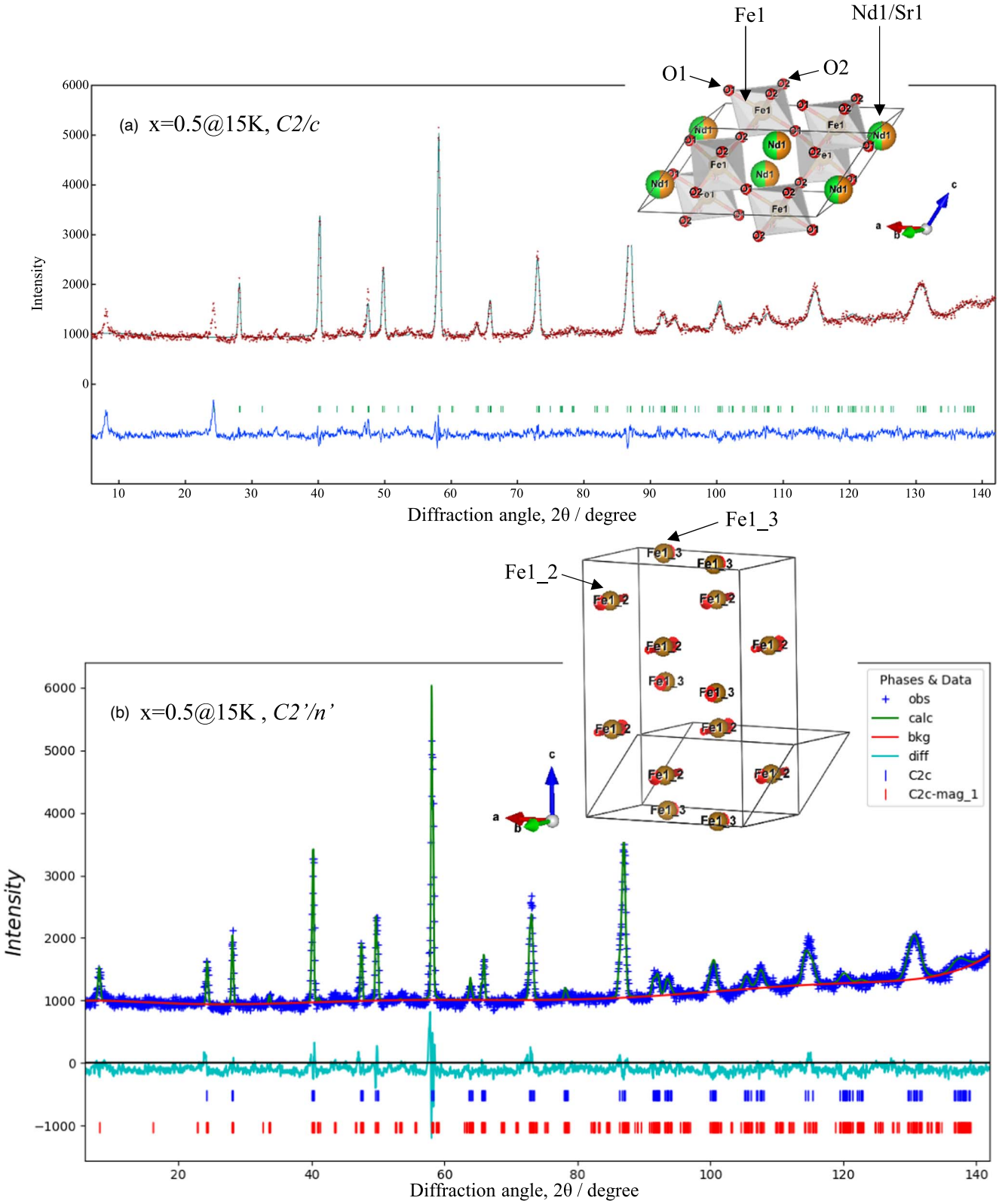

Fig. 5. (a) PND pattern and crystal structure, and (b) PND pattern and magnetic structure for $Nd_{0.5}Sr_{0.5}FeO_{3.00(2)}$ at 15 K.

susceptibility follows the Curie–Weiss law: $\chi - \chi_0 = C(T - \Theta)^{-1}$; thus, $(\chi - \chi_0)^{-1}$ is proportional to T, where the slope of the tangent is C^{-1} and $(\chi - \chi_0)^{-1}$ at $T = 0$ K is $-\Theta C^{-1}$, where C is the Curie constant and Θ is the Curie temperature. By calculating C from the slope of the tangent, we can estimate the effective magnetic moment μ_{eff} at the Fe site from

$$\mu_{\text{eff}} = \sqrt{\frac{3k_{\text{B}}C}{N_{\text{A}}}} = 2\sqrt{s(s+1)}\,\mu_{\text{B}}, \tag{2}$$

where s, k_{B}, and N_{A} are the spin quantum number, Boltzmann constant, and Avogadro's number, respectively. As shown in Figs. 3(a) and 3(b), the results for the samples with $x \leqslant 0.2$ at RT and those with $x \leqslant 0.7$ at low temperature show a good

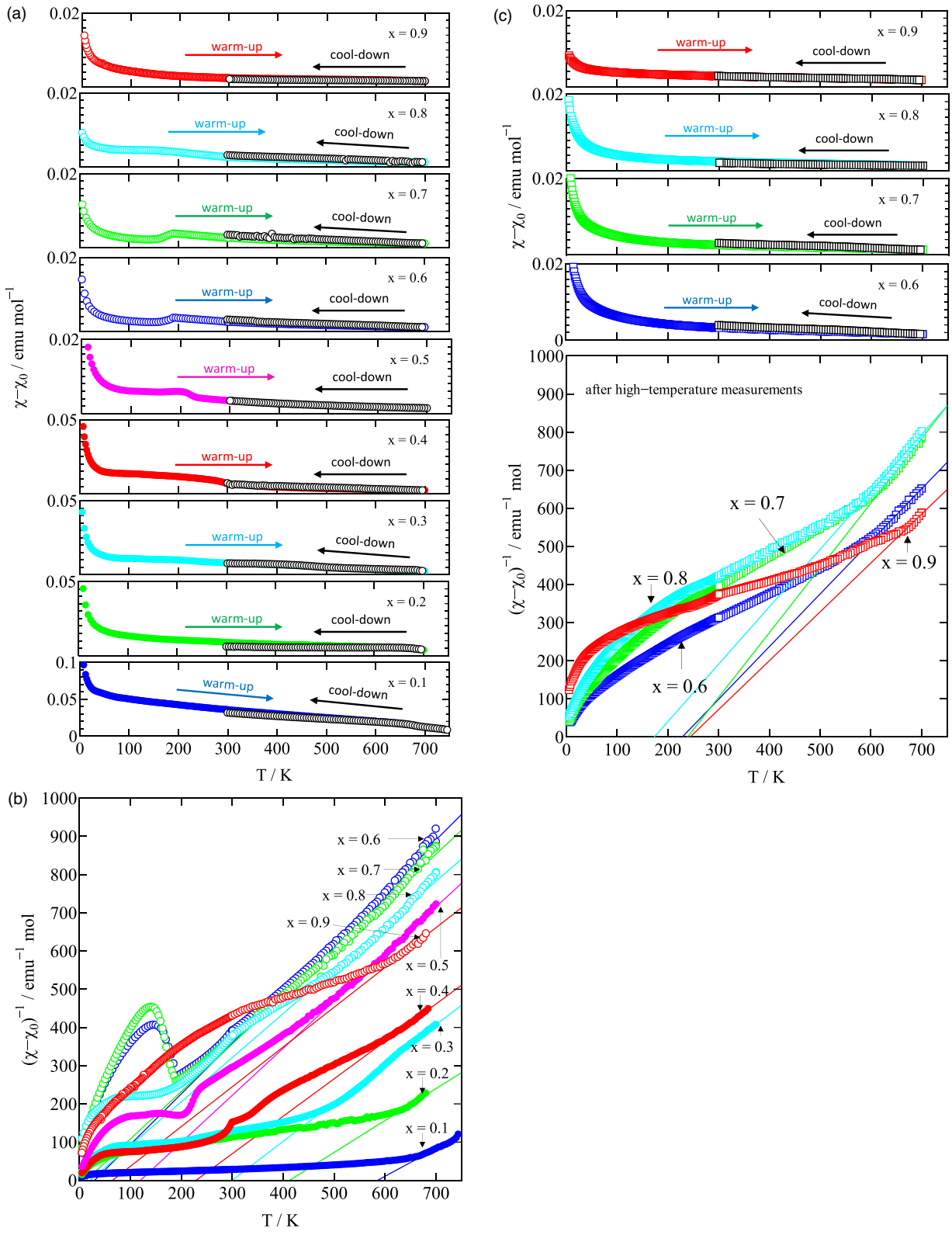

Fig. 6. (a) Temperature dependence of magnetic susceptibility, $\chi - \chi_0$ in both warm-up and cool-down processes, for $Nd_{1-x}Sr_xFeO_{3-\delta}$ ($0.1 \leqslant x \leqslant 0.9$) under zero-field cooling conditions in a magnetic field of 1 T, where the temperature-independent term, χ_0, is evaluated from χ ($T \to \infty$), as shown in the inset. (b) Temperature dependence of inverse magnetic susceptibility, $(\chi - \chi_0)^{-1}$ in the warm-up process, for $Nd_{1-x}Sr_xFeO_{3-\delta}$ ($0.1 \leqslant x \leqslant 0.9$). The straight lines represent the Curie–Weiss law at temperatures above 650 K. (c) Temperature dependence of magnetic susceptibility, $\chi - \chi_0$, in both warm-up and cool-down processes, and temperature dependence of inverse magnetic susceptibility, $(\chi - \chi_0)^{-1}$, in warm-up process for $Nd_{1-x}Sr_xFeO_{3-\delta}$ ($0.6 \leqslant x \leqslant 0.9$) after high-temperature measurement. The straight lines represent the Curie–Weiss law at temperatures above 650 K.

agreement between $|M|$ and μ_{eff}. In addition, as shown in Table II, because the spin quantum number at the Fe site is in the range $0.82 \leqslant x \leqslant 1.24$, the Fe site in $Nd_{1-x}Sr_xFeO_{3-\delta}$ is considered to be in the mixed-valence state of (IS $Fe^{3+}{}_{1-y}$ LS $Fe^{3+}{}_{y})_{1-(x-2\delta)}$ LS $Fe^{4+}{}_{x-2\delta}$, and the ratios among LS Fe^{3+}, IS Fe^{3+}, and LS Fe^{4+} can be determined. Table II summarizes χ_0, Θ, C, μ_{eff}, s, and the mixed-valence-state ratios for LS Fe^{3+}, IS Fe^{3+}, and LS Fe^{4+}. As x increases, the spin state of Fe changes from the LS or IS Fe^{3+}-dominant state at $x \leqslant 0.5$ to the LS Fe^{4+}-dominant state at $x \geqslant 0.6$. The

Table II. Temperature-independent magnetic susceptibility χ_0, paramagnetic Curie temperature Θ, Curie constant C, effective magnetic moment μ_{eff}, spin quantum number s, ionic ratio for Fe ions, Seebeck coefficient at high-temperature limit S_∞ obtained from Eq. (3), and Lorentz number L_0 for $Nd_{1-x}Sr_xFeO_{3-\delta}$ ($0.1 \leqslant x \leqslant 0.9$).

>Samples	$Nd_{1-x}Sr_xFeO_{3-\delta}$								
Composition, x	0.1	0.2	0.3	0.4	0.5	0.6	0.7	0.8	0.9
δ	0	0.004	0.01	0.011	0	0.01	0.009	0.035	0.048
χ_0 (emu mol^{-1})	0.000 04	0.000 56	0.000 93	0.001 62	0.002 05	0.001 73	0.001 84	0.001 56	0.001 03
Θ(K)	584	404	299	228	119	24	13	22	64
C (emu K mol^{-1})	1.382	1.198	0.983	1.021	0.811	0.753	0.805	0.867	0.961
μ_{eff} (μ_B)	3.325	3.095	2.804	2.857	2.547	2.453	2.537	2.633	2.772
Spin quantum number, s	1.24	1.13	0.99	1.01	0.87	0.82	0.86	0.91	0.97
LS Fe^{3+} ($s = 0.5$) (%)	21.4	27.8	37.1	29.7	38.2	38.5	29.6	22.7	12.5
IS Fe^{3+} ($s = 1.5$) (%)	68.6	53.0	34.9	32.5	11.8	3.5	2.2	4.3	7.1
LS Fe^{4+} ($s = 1.0$) (%)	10.0	19.2	28.0	37.8	50.0	58.0	68.2	73.0	80.4
S_∞ (μV K^{-1})	133.23	80.34	58.48	15.52	6.72	−2.73	−39.25	−69.80	−130.15
L_0 (V^2 K^{-2})	1.67×10^{-8}	2.15×10^{-8}	1.99×10^{-8}	2.33×10^{-8}	2.43×10^{-8}	2.44×10^{-8}	2.43×10^{-8}	2.42×10^{-8}	2.43×10^{-8}

increase in the amount of t_{2g} or e_g holes of LS Fe^{4+} with increasing x. This suggests that the major carriers change from t_{2g} or e_g holes in LS Fe^{4+} to t_{2g} electrons in LS Fe^{3+} or e_g electrons in IS Fe^{3+} as x increases.

Because the Seebeck coefficient at the high-temperature limit is estimated based on Eq. (1), S_∞ in the mixed-valence state of (IS $Fe^{3+}{}_{1-y}$ LS $Fe^{3+}{}_{y})_{1-(x-2\delta)}$ LS $Fe^{4+}{}_{x-2\delta}$ is expressed as

$$S_\infty \cong -\frac{k_B}{e}\left[y \ln\left\{\frac{6}{9}\frac{x-2\delta}{1-(x-2\delta)}\right\} + (1-y)\ln\left\{\frac{24}{9}\frac{x-2\delta}{1-(x-2\delta)}\right\}\right]. \quad (3)$$

As shown in Table II, S_∞ is estimated to be 133 μV K^{-1} from Eq. (3) for $Nd_{0.9}Sr_{0.1}FeO_{3.00(3)}$ ($y = 0.238$ and $\delta = 0.0$). However, S_∞ is estimated to be 130 μV K^{-1} for $Nd_{0.1}Sr_{0.9}FeO_{2.952(3)}$ ($y = 0.636$ and $\delta = 0.048$). Therefore, as shown in Fig. 7, S_∞ is expected to change from positive (p-type) to negative (n-type) with increasing x for calculation purposes. However, the oxygen-deficiency-induced changes in the electrical resistivity and Seebeck coefficient were confirmed at temperatures above 500 K in the samples with $0.6 \leqslant x \leqslant 0.9$. As shown in Fig. 6(c) and Table III, the results of $(\chi - \chi_0)^{-1}$ for $Nd_{1-x}Sr_xFeO_{3-\delta}$ ($0.6 \leqslant x \leqslant 0.9$) samples after high-temperature measurement show a substantial decrease in the ratio of LS Fe^{4+} and an increase in the ratio of LS Fe^{3+} and IS Fe^{3+}. This strongly suggests that Fe^{4+} is reduced to Fe^{3+} by the formation of an oxygen deficiency. Although the magnitude of the effective magnetic moment μ_{eff} has not substantially changed, the ratios of LS Fe^{3+}, IS Fe^{3+}, and LS Fe^{4+} have changed, resulting in S_∞ showing a positive (p-type) value, as represented by the open squares in Fig. 7.

Figure 8 shows the temperature dependence of the electrical resistivity ρ for $Nd_{1-x}Sr_xFeO_{3-\delta}$ ($0.1 \leqslant x \leqslant 0.9$) samples in the temperature range from 80 to 800 K. All the samples show semiconducting behavior over the entire temperature range, and ρ tends to decrease as x increases. In particular, ρ tends to decrease with increasing x until the composition $Nd_{0.5}Sr_{0.5}FeO_{3.00(2)}$ is reached; $Nd_{0.4}Sr_{0.6}FeO_{2.99(1)}$ shows an increasing trend, and $Nd_{0.3}Sr_{0.7}FeO_{2.991(9)}$, $Nd_{0.2}Sr_{0.8}FeO_{2.965(5)}$, and $Nd_{0.1}Sr_{0.9}FeO_{2.952(3)}$ show a decreasing tendency again with increasing x. However, oxygen deficiencies formed in $Nd_{0.4}Sr_{0.6}FeO_{2.99(1)}$, $Nd_{0.3}Sr_{0.7}FeO_{2.991(9)}$, $Nd_{0.2}Sr_{0.8}FeO_{2.965(5)}$, and $Nd_{0.1}Sr_{0.9}FeO_{2.952(3)}$ in the temperature range 500–600 K; their compositions therefore changed to $Nd_{0.4}Sr_{0.6}FeO_{2.824(2)}$, $Nd_{0.3}Sr_{0.7}FeO_{2.769(6)}$, $Nd_{0.2}Sr_{0.8}FeO_{2.71(1)}$, and $Nd_{0.1}Sr_{0.9}FeO_{2.62(1)}$, respectively. As a result, the electrical resistivity ρ increased by double digits and showed an irreversible temperature dependence because of the change of carriers from t_{2g} electrons in LS Fe^{3+} or e_g electrons in IS Fe^{3+} to t_{2g} holes or e_g holes in LS Fe^{4+} (Fig. 8).

Figure 9 shows the temperature dependence of S for $Nd_{1-x}Sr_xFeO_{3-\delta}$ ($0.1 \leqslant x \leqslant 0.9$) samples in the temperature range 170–800 K. p-type thermoelectric properties are observed for samples with $x \leqslant 0.5$, where $|S|$ decreases with increasing x. However, n-type thermoelectric properties are observed for samples with $x \geqslant 0.6$, where $|S|$ increases slightly with increasing x. By comparison with the x dependence of S_∞ calculated from Eq. (3), both Figs. 7 and 9 show that the thermoelectric characteristics change from p-type to n-type at $x = 0.6$ with increasing x. However, the results for

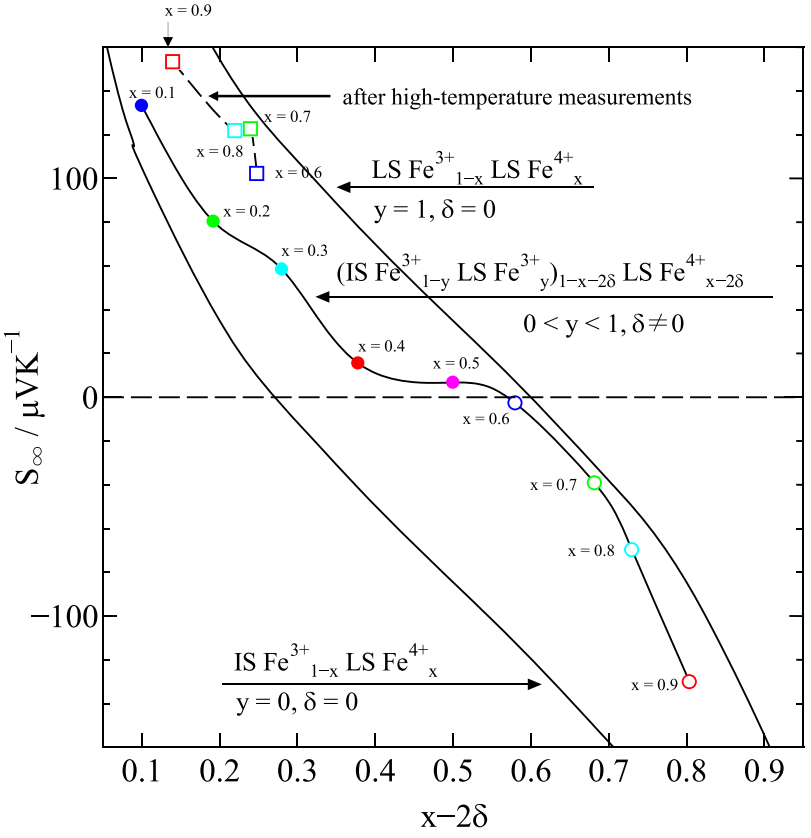

Fig. 7. Seebeck coefficient in the high-temperature limit, S_∞, for $Nd_{1-x}Sr_xFeO_{3-\delta}$ ($0.1 \leqslant x \leqslant 0.9$), where two solid curves, five solid circles , four open circles, and four open squares represent the relationship in Eq. (3).

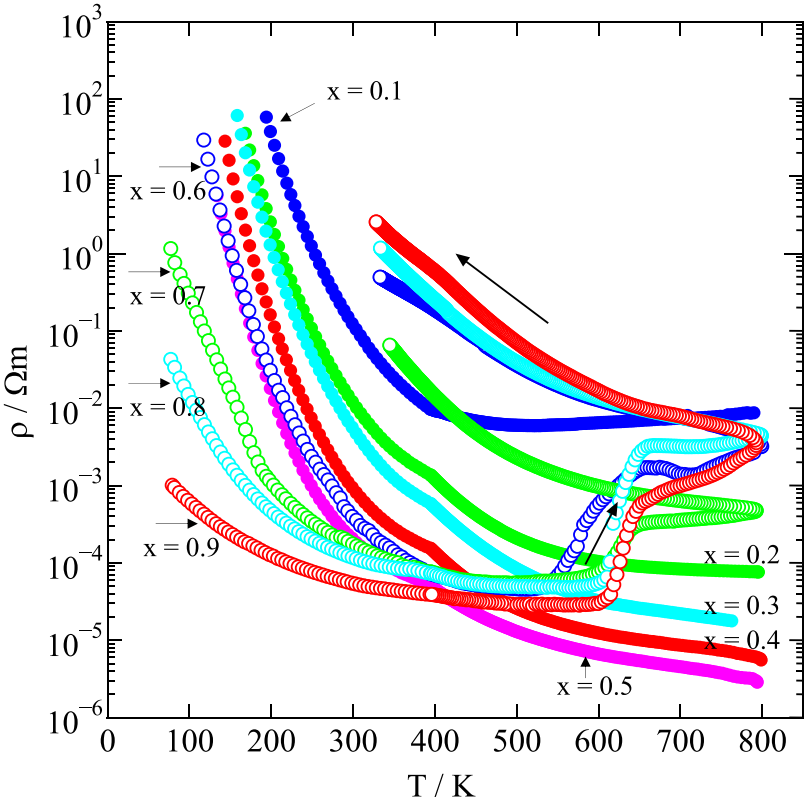

Fig. 8. Temperature dependence of electric resistivity, ρ, for $Nd_{1-x}Sr_xFeO_{3-\delta}$ ($0.1 \leqslant x \leqslant 0.9$).

Table III. Temperature-independent magnetic susceptibility χ_0, paramagnetic Curie temperature Θ, Curie constant C, effective magnetic moment μ_{eff}, spin quantum number s, ionic ratio for Fe ions, Seebeck coefficient at the high-temperature limit S_∞ obtained from Eq. (3), and Lorentz number L_0 for $Nd_{1-x}Sr_xFeO_{3-\delta}$ ($0.6 \leqslant x \leqslant 0.9$) after high-temperature measurement.

Samples	$Nd_{1-x}Sr_xFeO_{3-\delta}$			
Composition, x	0.6	0.7	0.8	0.9
δ	0.176	0.231	0.29	0.38
χ_0 (emu mol^{-1})	0.001 22	0.001 07	0.000 97	0.000 89
Θ(K)	23	9	16	52
C (emu K mol^{-1})	0.724	0.589	0.663	0.780
μ_{eff} (μ_B)	2.406	2.169	2.302	2.497
spin quantum number, s	0.80	0.69	0.75	0.84
LS Fe^{3+} ($s = 0.5$) (%)	57.3	68.6	63.4	58.5
IS Fe^{3+} ($s = 1.5$) (%)	17.9	7.4	14.6	27.5
LS Fe^{4+} ($s = 1.0$) (%)	24.8	24.0	22.0	14.0
S_∞ (μV K^{-1})	102.12	122.57	121.71	153.20
L_0 (V^2 K^{-2})	1.74×10^{-8}	2.36×10^{-8}	2.02×10^{-8}	2.25×10^{-8}

$Nd_{0.4}Sr_{0.6}FeO_{2.99(1)}$, $Nd_{0.3}Sr_{0.7}FeO_{2.991(9)}$, $Nd_{0.2}Sr_{0.8}FeO_{2.965(5)}$, and $Nd_{0.1}Sr_{0.9}FeO_{2.952(3)}$ show that Fe^{4+} is reduced to Fe^{3+} in the temperature range 500–600 K. Thus, the Seebeck coefficient S changes from negative (n-type) to positive (p-type) at temperatures greater than 600 K. As shown in Fig. 9, the Seebeck coefficient S for $0.6 \leqslant x \leqslant 0.9$ shows an irreversible temperature dependence and does not return to negative values (n-type) with decreasing temperature.

Figure 10 shows the temperature dependence of the total thermal conductivity κ ($=\kappa_L + \kappa_e$) and the carrier thermal conductivity κ_e for $Nd_{1-x}Sr_xFeO_{3-\delta}$ ($0.1 \leqslant x \leqslant 0.9$) samples in the temperature range 250–850 K, where κ_L is the lattice thermal conductivity and κ_e is calculated using the Wiedemann–Franz law ($\kappa_e = L_0\sigma T$). The Lorentz number L_0 is defined as[64]:

$$L_0 = \left(\frac{k_B}{e}\right)^2 \left[3\frac{F_2(\eta)}{F_0(\eta)} - 4\left(\frac{F_1(\eta)}{F_0(\eta)}\right)^2\right], \quad (4)$$

by assuming acoustic phonon scattering, where E_F is the Fermi energy, $\eta = \frac{E_F}{k_B T}$, and the function $F_n(\eta)$ is given by

$$F_n(\eta) = \int_0^\infty \frac{\chi^n}{1 + \exp(\chi - \eta)} d\chi, \quad (5)$$

where $\chi = \frac{E}{k_B T}$. The Seebeck coefficient S can be defined as

$$S = \pm\frac{k_B}{e}\left(2\frac{F_1(\eta)}{F_0(\eta)} - \eta\right); \quad (6)$$

thus, η is determined by fitting the experimental value of S at RT. The L_0 values calculated based on Eq. (4) are

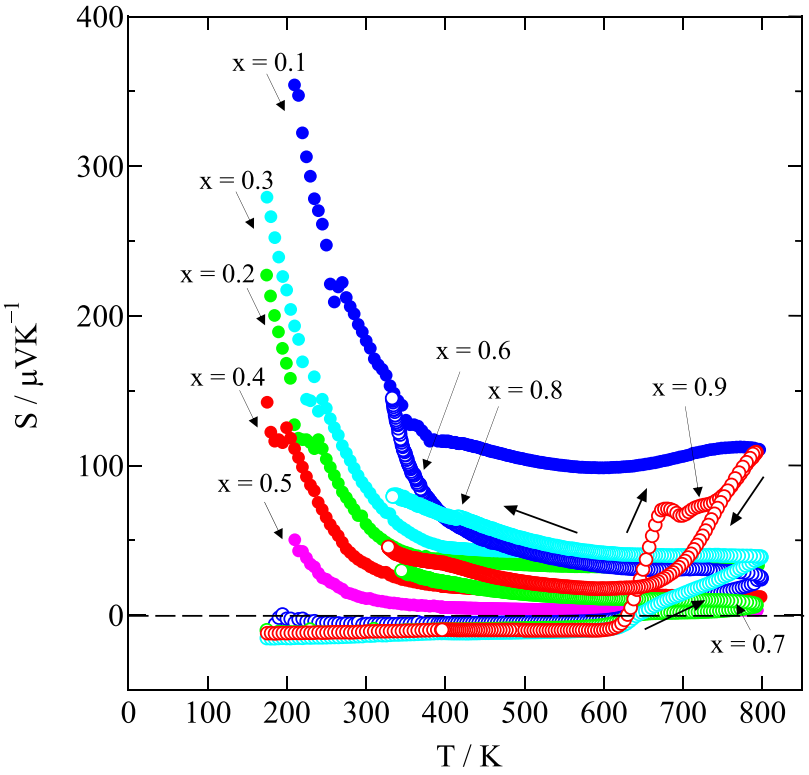

Fig. 9. Temperature dependence of the Seebeck coefficient, S, for $Nd_{1-x}Sr_xFeO_{3-\delta}$ ($0.1 \leqslant x \leqslant 0.9$).

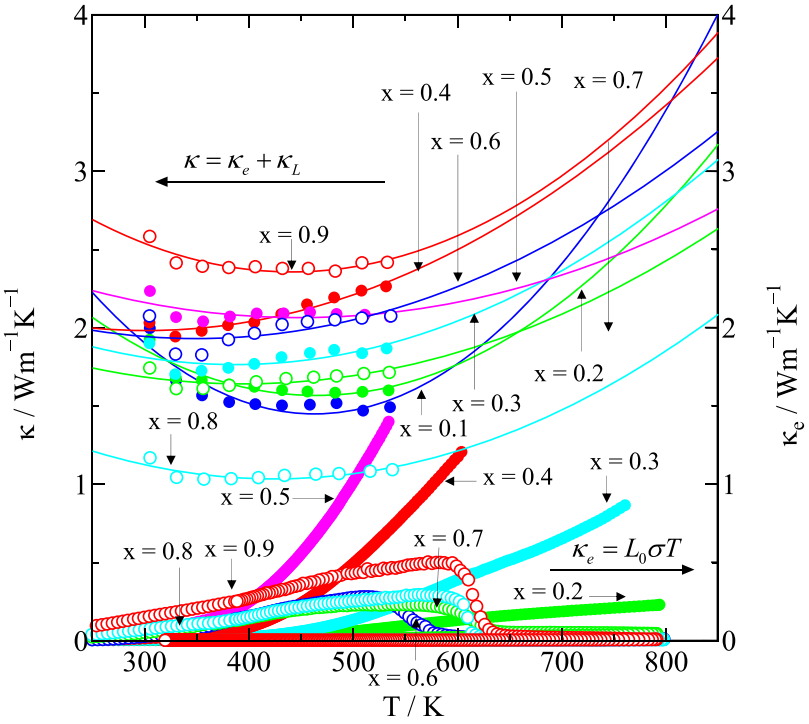

Fig. 10. Temperature dependence of the total thermal conductivity, $\kappa = \kappa_L + \kappa_e$ (left axis), and the temperature dependence of the carrier thermal conductivity according to the Wiedemann–Franz law, $\kappa_e = L_0\sigma T$ (right axis), at temperatures greater than RT for $Nd_{1-x}Sr_xFeO_{3-\delta}$ ($0.1 \leqslant x \leqslant 0.9$).

summarized in Tables II and III. As shown in Fig. 10, κ_e increases monotonically with increasing temperature; however, the ratio of κ_e to κ is relatively tiny compared with that of κ_L to κ. In particular, the oxygen deficiency is believed to have reduced LS Fe^{4+} to IS Fe^{3+} or LS Fe^{3+} for samples with $x > 0.6$, changing the conduction carriers from electrons to holes, and then increasing the resistivity with increasing temperature. κ_e of samples with $x > 0.6$ falls between 550 and 600 K due to the increase in the resistivity. Therefore, κ of the samples with $x > 0.6$ is expected to change to a decreasing trend above 550 K. However, for all the samples, κ_L plays a more critical role than κ_e, i.e. κ is mainly

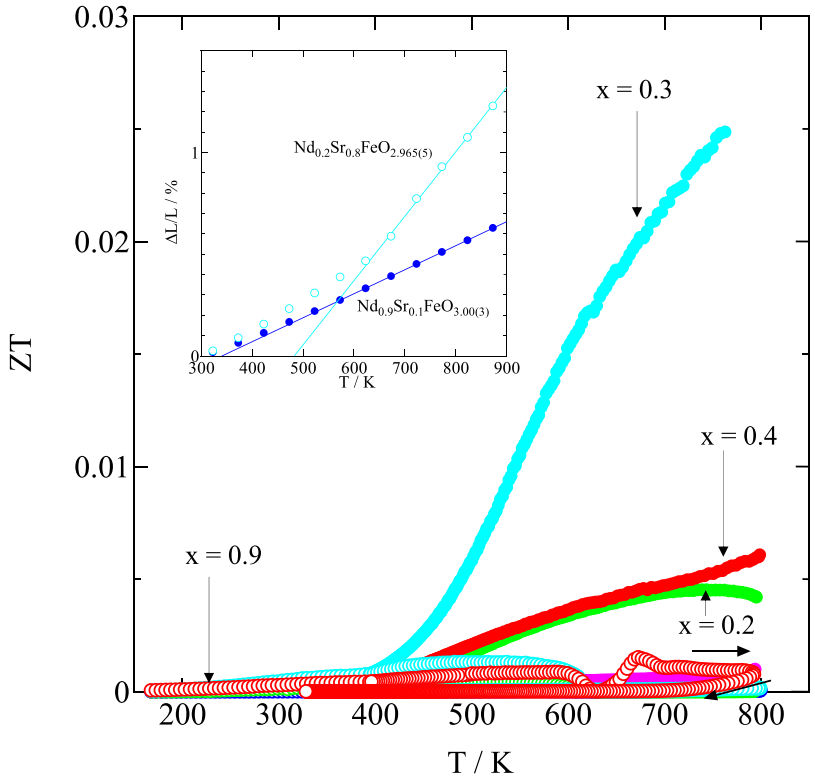

Fig. 11. Temperature dependence of the dimensionless figure of merit, *ZT*, for $Nd_{1-x}Sr_xFeO_{3-\delta}$ ($0.1 \leqslant x \leqslant 0.9$); the insets show the temperature dependence of the coefficients of linear thermal expansion for $Nd_{0.9}Sr_{0.1}FeO_{3.00(3)}$ and $Nd_{0.2}Sr_{0.8}FeO_{2.965(5)}$.

dominated by κ_L so that the value of κ remains relatively small for all the samples ($\kappa \leqslant 2.5\ Wm^{-1}\ K^{-1}$) over the whole temperature range.

Figure 11 shows the temperature dependence of the dimensionless figure of merit $ZT = S^2\sigma T\kappa^{-1}$ for $Nd_{1-x}Sr_xFeO_{3-\delta}$ ($0.1 \leqslant x \leqslant 0.9$) samples in the temperature range 170–800 K. In particular, $Nd_{0.7}Sr_{0.3}FeO_{2.99(1)}$ shows the highest *p*-type *ZT* value (i.e. $ZT = 0.025$ at 765 K). $Nd_{0.8}Sr_{0.2}FeO_{2.996(4)}$ and $Nd_{0.6}Sr_{0.4}FeO_{2.989(8)}$ also exhibit *p*-type *ZT* values (i.e. $ZT = 0.004$ at 800 K and $ZT = 0.006$ at 800 K, respectively). By contrast, $Nd_{0.4}Sr_{0.6}FeO_{2.99(1)}$, $Nd_{0.3}Sr_{0.7}FeO_{2.991(9)}$, $Nd_{0.2}Sr_{0.8}FeO_{2.965(5)}$, and $Nd_{0.1}Sr_{0.9}FeO_{2.952(3)}$ show a reduction of Fe^{4+} to Fe^{3+} in the temperature range 500–600 K, and the electrical resistivity ρ increases by double digits. In addition, because *S* changes from *n*-type to *p*-type at temperatures above ~600 K, Fe oxide compositions showing high *n*-type *ZT* values could not be identified. As shown in the inset of Fig. 11, the coefficients of linear thermal expansion at $T \geqslant 600$ K for $Nd_{0.9}Sr_{0.1}FeO_{3.00(3)}$ and $Nd_{0.2}Sr_{0.8}FeO_{2.965(5)}$ are $11.8 \times 10^{-6}\ K^{-1}$ and $28.9 \times 10^{-6}\ K^{-1}$, respectively. These results strongly suggest that $Nd_{0.2}Sr_{0.8}FeO_{2.965(5)}$ exhibits an increased linear thermal expansion coefficient because of the formation of oxygen deficiencies in the temperature range of 500–600 K, even under air. Therefore, fabricating a thermoelectric module that operates at high temperatures with *pn* elements requires the development of additional perovskite-type Fe oxides that exhibit similar linear thermal expansion coefficients and thermoelectric properties without forming oxygen deficiencies in the temperature range of 500–600 K.

4. Conclusions

The present study prepared polycrystalline $Nd_{1-x}Sr_xFeO_{3-\delta}$ ($0.1 \leqslant x \leqslant 0.9$) samples using a conventional solid-state reaction method. All the samples exhibited a typical single-phase perovskite structure. At 500 K and RT, the crystal structure corresponded to the monoclinic phase ($P2_1/m$) for $x = 0.1$ and 0.2, and the orthorhombic phase (*Pnma*) for $x \geqslant 0.3$. At low temperatures ($10\ K \leqslant T \leqslant 15\ K$), the monoclinic phase ($P2_1/m$) for $x = 0.1$ and 0.2, the orthorhombic phase (*Pnma*) for $x = 0.3$ and 0.4, and the monoclinic phase (*C*2/*c*) for $x \geqslant 0.5$ were identified. With increasing *x*, the Goldschmidt tolerance factor increases from 0.93 ($x = 0.1$) to 1.00 ($x = 0.9$) and the Fe–O–Fe angle also increases, reaching approximately 170°–180° at $x \geqslant 0.8$. These results strongly suggest that the strain in the FeO_6 oxygen octahedron tends to be relaxed with increasing *x*. However, the magnetic structure shows G-type antiferromagnetism with small ferromagnetic order in the *c*-axis direction for $x \leqslant 0.3$ and the *a*- or *b*-axis direction for $0.4 \leqslant x \leqslant 0.8$ at room or low temperature. Assuming that the Fe site is in the mixed-valence state of $(IS\ Fe^{3+}{}_{1-y}\ LS\ Fe^{3+}{}_{y})_{1-x-2\delta}\ LS\ Fe^{4+}{}_{x-2\delta}$, the spin state of Fe changes from the LS or IS Fe^{3+}-dominant state at $x \leqslant 0.5$ to the LS Fe^{4+}-dominant state at $x \geqslant 0.6$. This change suggests that the charge carriers change from t_{2g} or e_g holes in LS Fe^{4+} at $x \leqslant 0.5$ (*p*-type) to t_{2g} electrons in LS Fe^{3+} or e_g electrons in IS Fe^{3+} at $x \geqslant 0.6$ (*n*-type). In fact, at temperatures below 500 K, these samples show a *p*-type Seebeck coefficient when $0.1 \leqslant x \leqslant 0.5$ and an *n*-type Seebeck coefficient when $0.6 \leqslant x \leqslant 0.9$. However, for the $0.6 \leqslant x \leqslant 0.9$ samples, Fe^{4+} is reduced to Fe^{3+} because of oxygen deficiencies in the 500 to 600 K temperature range. The Seebeck coefficient for $0.6 \leqslant x \leqslant 0.9$ changes from negative (*n*-type) to positive (*p*-type) at temperatures greater than 600 K, and the electrical resistivity increases by two orders of magnitude and shows an irreversible temperature dependence. By contrast, the thermal conductivity remains relatively small, at $2.5\ Wm^{-1}\ K^{-1}$ or less for all the samples. As a result, $Nd_{0.7}Sr_{0.3}FeO_{2.99(1)}$ showed the highest

p-type *ZT* value (i.e. $ZT = 0.025$ at 765 K), although Fe oxide compositions with high *n*-type *ZT* values could not be identified. In addition, the coefficients of linear thermal expansion at $T \geqslant 600$ K for $Nd_{0.9}Sr_{0.1}FeO_{3.00(3)}$ and $Nd_{0.2}Sr_{0.8}FeO_{2.965(5)}$ are 11.8×10^{-6} K^{-1} and 28.9×10^{-6} K^{-1}, respectively. These results strongly suggest that the coefficient of linear thermal expansion for $Nd_{0.2}Sr_{0.8}FeO_{2.965(5)}$ increased because of oxygen deficiency in the temperature range of 500–600 K, even under air. Therefore, the fabrication of a thermoelectric module that operates at high temperatures with *pn* elements composed of perovskite-type Fe oxides will require the further development of perovskite-type Fe oxide compositions that exhibit similar linear thermal expansion coefficients and show *p*-type and n-type thermoelectric properties without becoming oxygen deficient in the temperature range 500–600 K.

Acknowledgments

This work was partly supported by a Grant-in-Aid for Scientific Research (19K04986). In addition, the magnetization measurement experiment below RT was carried out using the S700X-R equipment of the Yokohama National University Instrumental Analysis and Evaluation Center. The magnetization measurement experiments above RT were carried out using the MPMS equipment in the electromagnetic measurement room as a joint use of the University of Tokyo Physical Institute Laboratory. The PND measurements at 500 K, room, and low temperatures were carried out using the MEREDIT at the Nuclear Physics Institute, reactor LVR-15, Czech Republic.

1) W. M. Yim and F. D. Rosi, Solid-State Electron. **15**, 1121 (1972).
2) S. Yoneda, E. Ohta, H. Kaibe, I. Ohsugi, Y. Shinohara, and I. Nishida, J. Adv. Sci. **12**, 379 (2000).
3) C. B. Vining, J. Appl. Phys. **69**, 331 (1991).
4) J. S. Dick, W. Chen, C. Uher, L. Chen, X. Tang, and T. Hirai, J. Appl. Phys. **91**, 3698 (2002).
5) X. Shi, H. Kong, C.-P. Li, C. Uher, J. Yangu, J. R. Salavador, H. Wang, L. Chen, and W. Zhang, Appl. Phys. Lett. **92**, 182101 (2008).
6) I. Nishida, Phys. Rev. **B7**, 2710 (1973).
7) I. Ohsugi, T. Kojima, M. Sakata, and I. Nishida, J. Jpn. Inst. Met. **58**, 985 (1994).
8) I. Terasaki, Y. Sasago, and K. Uchinokura, Phys. Rev. **B56**, R12685 (1997).
9) A. C. Masset, C. Michel, A. Maignan, M. Hervien, O. Toulemonde, F. Studer, and B. Raveau, Phys. Rev. B **62**, 166 (2000).
10) Y. Miyazaki, K. Kudo, M. Akoshima, Y. Ono, Y. Koike, and T. Kajitani, Jpn. J. Appl. Phys. **39**, L531 (2000).
11) P. Bollay, B. Domenges, M. Hervieu, D. Groult, and B. Raveau, Chem. Mater. **8**, 1482 (1996).
12) S. Hebert, S. Lambert, D. Pelloquin, and A. Maignan, Phys. Rev. B **64**, 172101 (2001).
13) D. Pelloquin, A. Maignan, S. Hebert, C. Martin, M. Hervieu, C. Michel, L. B. Wang, and B. Raveau, Chem. Mater. **14**, 3100 (2002).
14) D. Pelloquin, A. Maignan, S. Hebert, C. Martin, and B. Raveau, J. Solid State Chem. **170**, 374 (2003).
15) Y. Miyazaki, T. Miura, Y. Ono, and T. Kajitani, Jpn. J. Appl. Phys. **41**, L849 (2002).
16) M. Hervieu, Ph. Boullay, C. Michel, A. Maignan, and B. Raveau, J. Solid State Chem. **142**, 305 (1999).
17) T. Itoh and I. Terasaki, Jpn. J. Appl. Phys. **39**, 6658 (2000).
18) M. Hervieu, A. Maignan, C. Michel, V. Hardy, N. Creon, and B. Raveau, Phys. Rev. B **67**, 045112 (2003).
19) K. Sakai, M. Karppinen, J. M. Chen, R. S. Liu, S. Sugihara, and H. Yamauchi, Appl. Phys. Lett. **88**, 232102 (2006).
20) T. Motohashi, Y. Nonaka, K. Sakai, M. Karppinen, and H. Yamauchi, J. Appl. Phys. **103**, 033705 (2008).
21) M. Ohtaki, T. Tsubota, K. Eguchi, and H. Arai, J. Appl. Phys. **79**, 1816 (1996).
22) T. Tsubota, M. Ohtaki, K. Eguchi, and H. Arai, J. Mater. Chem. **7**, 85 (1997).
23) T. Tsubota, M. Ohtaki, K. Eguchi, and H. Arai, J. Mater. Chem. **8**, 409 (1998).
24) T. Kobayashi, H. Takizawa, T. Endo, T. Sato, M. Shimada, H. Taguchi, and M. Nagao, J. Solid State Chem. **92**, 116 (1991).
25) M. Ohtaki, H. Koga, T. Tokunaga, K. Eguchi, and H. Arai, J. Solid State Chem. **120**, 105 (1995).
26) D. Flahaut, T. Mihara, R. Funahashi, N. Nabeshima, K. Lee, H. Ohta, and K. Koumoto, J. Appl. Phys. **100**, 084911 (2006).
27) X. Y. Huang, Y. Miyazaki, and T. Kajitani, Solid State Commun. **145**, 132 (2008).
28) S.-M. Choi, C.-H. Lim, and W.-S. Seo, J. Electron. Mater. **40**, 551 (2011).
29) P. Thiel, S. Populoh, S. Yoon, and A. Weidenkaff, J. Solid State Chem. **229**, 62 (2015).
30) S. Paengson, P. Pilasuta, K. Singsoog, W. Namhongsa, W. Impho, and T. Seetawan, Mater. Today: Proc. **4**, 6289 (2017).
31) S. de O. A. Torres, D. Thomazini, G. P. Balthazar, and M. V. Gelfuso, Mater. Res. **23**, 1 (2020).
32) A. Vijay, S. Charan Prasanth, R. Jose, P. Vineetha, and K. Venkata Saravanan, Cryst. Res. Technol. **57**, 2200041 (2022).
33) S. Ohta, T. Nomura, H. Ohta, and K. Koumoto, J. Appl. Phys. **97**, 034106 (2005).
34) S. Ohta, T. Nomura, H. Ohta, M. Hirano, H. Hosono, and K. Koumoto, Appl. Phys. Lett. **87**, 092108 (2005).
35) S. Ohta, H. Ohta, and K. Koumoto, J. Ceram. Soc. Jpn. **114**, 102 (2006).
36) K. Kato, M. Yamamoto, and S. Ohta, J. Appl. Phys. **102**, 116107 (2007).
37) H. Wang and C. Wang, Ceram. Int. **39**, 941 (2013).
38) H. Somaily, S. Kolesnik, B. Dabrowski, and O. Chmaissem, Phys. Rev. B **96**, 064105 (2017).
39) T. T. Khan, I.-H. Kim, and S.-C. Ur, J. Electron. Mater. **48**, 1864 (2019).
40) S. Charan Prasanth, J. Roshan, V. Ammu, P. Vineetha, and K. Venkata Saravanan, Mater. Today: Proc. **64**, 464 (2022).
41) M. Iijima and N. Murayama, Proc. Int. Conf. Thermoelectr. ICT98 **17**, 598 (1998).
42) K. Kobayashi, S. Yamaguchi, T. Tsunoda, and Y. Imai, Solid State Ionics **144**, 123 (2001).
43) M. V. Patrakeev, E. B. Mitberg, A. A. Lakhtin, I. A. Leonidov, V. L. Kozhevnikov, V. V. Kharton, M. Avdeev, and F. M. B. Marques, J. Solid State Chem. **167**, 203 (2002).
44) K. Iwasaki, T. Ito, M. Yoshino, T. Matsui, T. Nagasaki, and Y. Arita, J. Alloys Compd. **430**, 297 (2007).
45) H. C. Wang, C. L. Wang, J. L. Zhang, W. B. Su, J. Liu, M. L. Zhao, N. Yin, Y. G. Lv, and L. M. Mei, Curr. Appl. Phys. **10**, 866 (2010).
46) J. Androulakis, P. Migiakis, and J. Giapintzakis, Appl. Phys. Lett. **84**, 1099 (2004).
47) K. Iwasaki, T. Ito, T. Nagasaki, Y. Arita, M. Yoshino, and T. Matsui, J. Solid State Chem. **181**, 3145 (2008).
48) H. Hashimoto, T. Kusunose, and T. Sekino, J. Alloys Compd. **484**, 246 (2009).
49) K. H. Jung, S.-M. Choi, H. H. Park, and W.-S. Seo, Curr. Appl. Phys. **11**, S260 (2011).
50) V. Vulchev, L. Vassilev, S. Harizanova, M. Khristov, E. Zhecheva, and R. Stoyanova, J. Phys. Chem. C **116**, 13507 (2012).
51) M. A. Bousnina, R. Dujardin, L. Perriere, F. Glovannelli, G. Guegan, and F. Delorme, J. Adv. Ceram. **7**, 160 (2018).
52) V. A. Dudnikov, Y. S. Orlov, N. V. Kazak, A. S. Fedorov, L. A. Solov'yov, S. N. Vereshchagin, A. T. Burkov, S. V. Novikov, and S. G. Ovchinnikov, Ceram. Int. **45**, 5553 (2019).
53) M. A. Bousnina, F. Glovannelli, L. Perriere, G. Guegan, and F. Delorme, J. Adv. Ceram. **8**, 519 (2019).
54) V. A. Dudnikov, A. S. Fedorov, Y. S. Orlov, L. A. Solovyov, S. N. Verexhchagin, S. Y. Gavrilkin, A. Y. Tsvetkov, M. V. Gorev, S. V. Novikov, and S. G. Ovchinnikov, Ceram. Int. **46**, 17987 (2020).
55) W. Koshibae, K. Tsutsui, and S. Maekawa, Phys. Rev. **B62**, 6869 (2000).
56) H. Nakatsugawa, M. Saito, and Y. Okamoto, Mater. Trans. **60**, 1051 (2019).
57) F. Izumi and K. Momma, Solid State Phenom. **130**, 15 (2007).
58) A. C. Larson and R. B. Von Dewwlw, General Structure Analysis System (GSAS) Report LAUR 86-748 Los Alamos National Laboratory, 2004.
59) K. Momma and F. Izumi, J. Appl. Cryst. **41**, 653 (2008).
60) C. J. Howard and H. T. Stokes, Acta Cryst. **B58**, 565 (2002).
61) I. Khanna and N. K. Verma, J. Magn. Magn. Mater. **336**, 1 (2013).
62) R. V. K. Mangalam, N. Ray, U. V. Waghmare, A. Sundaresan, and C. N. R. Rao, Solid State Commn. **149**, 1 (2009).
63) T. Osaka, H. Takahashi, H. Sagayama, Y. Yamasaki, and S. Ishiwata, Phys. Rev. **B95**, 224440 (2017).
64) L. D. Zhao et al., J. Am. Chem. Soc. **133**, 20476 (2011).

